STUDY OF $BiFeO_3$ INCORPORATION IN STRUCTURAL, DIELECTRIC AND FERROELECTRIC PROPERTIES OF $BaTiO_3$ CERAMICS

A DISSERTATION

Submitted in partial fulfillment of the requirements for the award of the degree

of

MASTER OF TECHNOLOGY

in

SOLID STATE ELECTRONIC MATERIALS

By

ARVIND KUMAR

DEPARTMENT OF PHYSICS
INDIAN INSTITUTE OF TECHNOLOGY ROORKEE
ROORKEE -247 667 (INDIA)

JUNE, 2014

Dedicated to

My Loving Parents

CANDIDATE'S DECLARATION

I hereby declare that the work presented in this dissertation report entitled **"Study of $BiFeO_3$ Incorporation on Structural, Dielectric and Ferroelectric Properties of $BaTiO_3$ Ceramics"** for the partial fulfillment of the requirements for the award of the degree of **"Master of technology"** in "**Solid State Electronic Materials**" is submitted in the Department of Phyiscs, Indian Institute of Technology Roorkee. This report is an authentic record of my own work carried out under the supervision and guidance of **Prof. Davinder Kaur**, Department of Physics, Indian Institute of Technology, Roorkee.

The matter embodied in this report work has not been submitted for the award of any other degree.

Date 16/06/14

Place : Roorkee **(Arvind Kumar)**

CERTIFICATE

This is to certify that the work related to dissertation entitled ""**Study of $BiFeO_3$ Incorporation on Structural, Dielectric and Ferroelectric Properties of $BaTiO_3$ Ceramics**" carried out by **Mr. Arvind Kumar** under my supervision for the partial fulfillment of **"Master of Technology"** with specialization in **"Solid State Electronic Materials".**

Date: June 16, 2014

Place: Roorkee

Prof. Davinder Kaur
Department of Physics
Indian Institute of Technology
Roorkee-247667, India

ACKNOWLEDGEMENTS

First and foremost, I would like to express my deep and sincere gratitude to my supervisor, Prof. Davinder Kaur (Dept. of Physics, Indian Institute of Technology Roorkee), who supported me throughout my M.Tech Dissertation with her valuable guidance, indefatigable inspiration, cogent discussion and immense knowledge. She always provides me enough resources and freedom to work in my own way. She was always available for me to give the helpful guidance and strong support whenever I was needed. Not in the academics but also in my personal life she had made a great influence on me. I was the most fortunate to have her as my supervisor.

I am thankful to Prof. A.K. Jain, Head of Department, Physics Department for providing me the necessary facilities to complete this dissertation work.

I am deeply grateful to Prof. Ramesh Chandra, Institute Instrumentation Center, IIT Roorkee, who has allowed me to use the facilities of his lab and of Institute Instrumentation Center necessary for the completion of this dissertation work.

My appreciation also goes to all my lab mates who supported me by giving their valuable suggestions. I thank them all for their full co-operation and for also being around all time.

I am grateful to all my friends who always supported me and encourage me in many ways that cannot be expressed in words.

The financial help provided by Ministry of Human Resource Development (MHRD), Govt. of India is thankfully acknowledged.

Finally, I have no words to express my deepest appreciation to my family members, for their understanding and support during all these years. I could not have reached this important milestone of my life without their support and encouragement.

(Arvind Kumar)

ABSTRACT

Perovskite $BaTiO_3$ was prepared by the solid state reaction method with the materials $BaCO_3$ and TiO_2. The calcinations were carried out at 1150^0C for 4 hrs. To study the structural, dielectric and ferroelectric properties of $BaTiO_3$ ceramics, the sintering was carried out at 1100^0C, 1200^0C and 1300^0C for 4 hrs respectively. The XRD analysis shows the single phase tetragonal perovskite of $BaTiO_3$ ceramics without any second phase. The average grain size increased from 0.20μm to 0.70μm on increasing the sintering temperature. The dielectric properties i.e., dielectric constant 'ε_r' and dielectric loss 'tanδ' are investigated and found to be large ε_r and low loss; the ferroelectric properties (i.e., remnant polarization and the coercive field) were also investigated and found to be large polarization.

A single-phase multiferroic ceramics of (1 – x) $BiFeO_3$ - x $BaTiO_3$ (BFO – x BTO) were also prepared by the solid state reaction method with wide range of the material composition (x = 0.1 – 1.0). This BFO with BTO shows structural transformations over the entire compositional range. These transformations were confirmed by the X-ray diffractions (XRD). Below x=0.3 BFO shows rhombohedral structure, above this composition it shows cubic structure and above 90% of BTO the structure becomes tetragonal. The ferroelectric Curie temperature T_C decreases with increasing of BTO concentration, which shows small relaxation. Average grain size first increases and then decreases that is found large for 0.5 BF- 0.5 BT composite. The dielectric constant enhances as BTO content increases. The polarization first increases and becomes maximum for x=0.3, after that it starts decrease with the increasing of the BTO concentration. This suggested that the morphotropic phase boundary (MPB) exist at this composition that means the rhombohedral and cubic phases coexist for 0.7BF - 0.3BT composite.

CONTENTS

CANDIDATE'S DECLARATION	ii
CERTIFICATE	ii
ACKNOWLEDGMENTS	iii
ABSTRACT	iv
LIST OF FIGURE	viii-x
LIST OF TABLES	xi
CONTENTS	

CHAPTER – 1 INTRODUCTION 1 - 3

1.1 Motivation

1.2 Outline of Thesis

1.3 References

CHAPTER – 2 LETERATURE REVIEW 4 - 18

2.1 Multiferroics

2.1.1 Ferroelectricity

2.1.2 Ferromagnetism

2.1.3 Multiferroism

2.2 Magnetoelectric Effect

2.3 Perovskite Structure

2.4 Barium Titanate ($BaTiO_3$)

2.5 Bismuth Ferrite ($BiFeO_3$)

2.6 References

CONTENTS

CHAPTER – 3 SYNTHESIS AND CHARACTERIZATION TECHNIQUES 19 - 34

3.1 Solid State Reaction Method

3.2 Samples Preparation

3.2.1 Synthesis of $BiFeO_3$ (BFO)

3.2.2 Synthesis of (1-x) BiFeO3 (BFO) – $xBaTiO_3$ (BTO) composites

3.2.3 Synthesis of $BaTiO_3$ (BTO)

3.3 The Structural Characterization Techniques

3.3.1 X-Ray Diffraction (XRD)

3.3.2 Field Emission Scanning Electron Microscopy (FE-SEM)

3.4 Dielectric Measurement

3.5 Ferroelectric Measurement

3.6 Differential Thermal Analysis

3.7 References

CHAPTER – 4 RESULTS AND DISCUSSIONS 35 - 59

4.1 Characterizations of the $BaTiO_3$ ceramic

4.1.1 Structural Studies by XRD

4.1.2 Surface Morphology Analysis

4.1.3 Dielectric Properties

4.1.4 Ferroelectric Properties

4.2 Characterizations of the (1-x) $BiFeO_3$ - $xBaTiO_3$ composites

4.2.1 Structural Studies by XRD

4.2.2 Surface Morphology Analysis

4.2.3 Dielectric Properties

4.2.4 Ferroelectric Properties

4.3 References

CHAPTER – 5 CONCLUSIONS 60

LIST OF FIGURES

CHAPTER - 2

Figure 1.1 Condition for the existence of the dipole moment.

Figure 1.2 Ferroelectric hysteresis loop (P-E loop).

Figure 1.3 Different types of magnetic ordering.

Figure 1.4 Interactions in multiferroic materials.

Figure 1.5 Schematic of Perovskite Structure.

Figure 1.7 (a) Unit cell of $BaTiO_3$ (b) Ion displacement due to the cubic-tetragonal distortion in $BaTiO_3$ (c) The temperature dependence of $BaTiO_3$ structure.

Figure 1.8 The crystal structure of the bulk $BiFeO_3$.

Figure 1.9 A part of $BiFeO_3$ lattice with the iron and the oxygen ions, the arrows show Fe^{3+} moment direction.

CHAPTER - 3

Figure 3.1 Diffraction of X-rays by crystal planes.

Figure 3.2 Effect of grain size on X-ray diffraction peak.

Figure 3.3 X-ray diffractometer (Bruker AXS, D8 Advance), IIC, IIT Roorkee.

Figure 3.4 Schematic diagram of the Field Emission Scanning Electron Microscope.

Figure 3.5 Interaction between electron beam and sample.

Figure 3.6 Field Emission Scanning Electron Microscope (FEI, Quanta 200F) at IIC.

Figure 3.7 (a) Agilent Impedance Analyzer, (b) Radiant Ferroelectric Test System.

Figure 3.8 Schematic of Sawyer – Tower circuit for the ferroelectric measurement.

Figure 3.9 Schematic diagram of the DTA.

Figure 3.10 Measurement principles of the DTA.

LIST OF FIGURES

CHAPTER - 4

Figure 4.1 XRD pattern of the $BaTiO_3$ sintered at 1100^0C.

Figure 4.2 XRD pattern of the $BaTiO_3$ sintered at 1200^0C.

Figure 4.3 XRD pattern of the $BaTiO_3$ sintered at 1300^0C.

Figure 4.4 Dependence of the lattice constants (a and c), and the c/a ratio (i.e. on right hand side) on the sintering temperature.

Figure 4.5 SEM micrographs of $BaTiO_3$ sintered at (a) 1100^0C, (b) 1200^0C, and (c) 1300^0C.

Figure 4.6 Dependence of the dielectric constant with temperature at various sintering temperature.

Figure 4.7 Dependence of the dielectric loss with temperature at different sintering temperature.

Figure 4.8 P-E loop of all $BaTiO_3$ samples prepared at different sintering temperatures.

Figure 4.9 Leakage current (Amps.) vs. time (ms) sintered at the various temperatures.

Figure 4.10 XRD patterns of (1-x) $BiFeO_3$ - $xBaTiO_3$ ceramics with compositions, x = 0 (BFO), 0.1 and 0.3.

Figure 4.11 XRD patterns of (1-x) $BiFeO_3$ - $xBaTiO_3$ ceramics with compositions, x = 0.5, 0.7 and 1.0.

Figure 4.12 XRD patterns at near 31.5^0 (a) for pure BFO, 0.1 BT and 0.3 BT, and (b) 0.5 BT, 0.7 BT and pure BT.

Figure 4.13 SEM micrographs of (1-x) BiFeO3 - $xBaTiO_3$ composites at (a) x = 0, (b) x = 0.1, (c) x = 0.3, (d) x = 0.5, (e) x = 0.7, and (e) x = 1.0.

Figure 4.14 The dependence of dielectric constants with temperature for all compositions.

Figure 4.15 Dependence of dielectric loss (tanδ) with the temperature for all compositions.

Figure 4.16 Differential thermal analysis graphs.

Figure 4.17 Hysteresis loops of polarization (P) vs. electric field (E) for (a) x=0, (b) x=0.1, (c) x=0.3, (d) x=0.5, (e) x=0.7, and (f) x=1.0.

Figure 4.18 Leakage current versus time of (1-x) BF-x BT ceramics (a) at x=0, 0.1, 0.3 and (b) at x=0.5, 0.7, 1.0.

LIST OF TABLES

Table 1. Lattice parameters calculated at various sintering temperature

Table 2. Crystallite Sizes calculated at various sintering temperature

Table 3. Average grain size calculated at different sintering temperatures

Table 4. The values of ε_r and tanδ at RT and T_C

Table 5. The values of P_s, P_r and E_C of BTO samples sintered at various temperatures

Table 6. Leakage current density for different samples

Table 7. The values of lattice constants, angle 'α' and particle size

Table 8. Average grain size for all compositions

Table 9. Dielectric constant and dielectric loss at room temperature

Table 10. The values of P_r, P_s and E_C

1.1 Motivation

The properties of ferroelectricity, piezoelectricity and ferromagnetism are shown by the materials like $BaTiO_3$ (or BTO), $BiFeO_3$ (or BFO) and BFO-BTO composites. These materials are used in various applications like capacitors, non volatile memories, FeRAM (ferroelectric random access memory), multilayer charged capacitors (MLCC) , magnetic sensors, transducers and spintronic ones [1- 3].

Out of the various ferroelectrics, the $BaTiO_3$ has a high dielectric constant and shows mostly the best ferroelectric properties. It is used for various applications because of its promising structural, dielectric, electrical and the ferroelectric properties [4-6]. The BTO based ferroelectric materials are also strong candidates for the piezoelectric transducers due to their large permittivity, large polarization and the large strains. Because it is a lead free ferroelectric material; therefore, it is an environmentally friendly material.

Bismuth ferrite ($BiFeO_3$) is the only multiferroic material that exhibits a microscopic coupling between the electric and magnetic ordering at the room temperature. It also shows good ferroelectric and the piezoelectric properties [7-9]. It is difficult to prepare the BFO ceramics with the pure perovskite structure [10] (i.e. a secondary or impurity phase is observed). The substitution of the ferroelectrics to the BFO can reduce the impurity phase.

Many researchers used the addition of $PbTiO_3$ in BFO to suppress the secondary phase. I used the BTO, which is a good ferroelectric, and it shows a tetragonal structure at room temperature. It is similar to that of $PbTiO_3$.

Many methods can be used to synthesize the BF-BT ceramics like wet chemical methods such as sol-gel method, co-precipitation, micro emulsion, hydrothermal and solid state reaction method. First three methods offer advantages such as phase purity, processibility, controlled stoichiometry and homogeneity, but still give serious problems like complicated washing conditions that is difficult to control. Sol-gel method requires precursors which are expensive and not commonly available.

Traditionally, solid state reaction method is used to prepare the BTO, and BFO-BTO composites. Out of these various methods solid state reaction method (SSR) is one of the most used method, because of its amenability to the large scale production [11-12] and can be easily

handled. The implication of these materials in any devices required a definite shape which can be given during sintering process.

1.2 Outline of Thesis

This thesis is divided into the 4 chapters; chapter 2 contains the literature review which includes the brief description of ferroelectricity, ferromagnetism, anti-ferromagnetism, and perovskite structure along with some necessary definitions related to these phenomenons as well as the brief introduction of $BaTiO_3$ and $BiFeO_3$ materials.

Chapter 3 includes the synthesis of BTO, (1-x) BFO-x BTO ceramics by solid state reaction method. It also covers the structural, dielectric, ferroelectric and differential thermal analysis (DTA) properties of these ceramics.

Chapter 4 includes the optimization of the BTO and (1-x) BFO-x BTO ceramics at different compositions of x. XRD, FESEM, differential thermal analysis (DTA), dielectric and ferroelectric properties shown by these composites are also included in results and discussion part of this chapter.

Chapter 5 contains the conclusions.

References:

[1]. M. M. VijatovićJ, D. Bobić, B. D. Stojanović, History and challenges of barium titanate: Part I, Science of Sintering 40 (2008) 155–165.

[2]. N. A. Spaldin, Science 309, 391 (2005).

[3]. H. Schmid, Ferroelectrics 162, 317 (1994).

[4]. B. Jaffe, W.R. Cook, Piezoelectric Ceramics, Academic Press, London, U.K., 1971.

[5]. G.H. Heartling, Ferroelectric ceramics: history and technology, J. Am. Ceram. Soc. 82 (1999) 797.

[6]. B.D. Stojanovic, V.R. Mastelaro, C.O. Paiva Santos, J.A. Varela, Structure study of donor doped barium titanate prepared from citrate solutions, Sci. Sintering 36 (2004) 179.

[7]. T. Takenaka, K. Maruyama, and K. Sakata, "$(Bi_{1/2}Na_{1/2})$ TiO_3–$BaTiO_3$ System for Lead-Free Piezoelectric Ceramics," Jpn. J. Appl. Phys., 30, 2236–9 (1991).

[8].X. X. Wang, X. G. Tang, and H. L. W. Chan, "Electromechanical and Ferroelectric Properties of $(Bi_{1/2}Na_{1/2})TiO_3$–$(Bi_{1/2}K_{1/2})TiO_3$–$BaTiO_3$ Lead-Free Piezoelectric Ceramics," Appl. Phys. Lett., 85, 91–3 (2004).

[9].M. R. Suchomel and P. K. Davies, "Enhanced Tetragonality in $xPbTiO_3$– (1-x) $Bi(Zn_{1/2}Ti_{1/2})O_3$ and Related Solid Solution Systems," Appl. Phys. Lett., 86, 262905, 3pp (2005).

[10]. G. Catalan and J. F. Scott, "Physics and Applications of Bismuth Ferrite," Adv. Mater., 21, 2463–85 (2008).

[11]. A.K. Jha, K.Prasad, Ferroelectric $BaTiO_3$ nanoparticles: biosynthesis and characterization, Colloids and Surfaces B: Biointerfaces75 (2010) 330–334.

[12]. P. Yu, X.Wang, B.Cui, Preparation and characterization of $BaTiO_3$ powders and ceramics by the sol–gel process using organic monoacid as surfactant, Scripta Materialia 57 (2007) 623–626.

2.1 Multiferroics

Multiferroics are the materials that exhibit more than two ferroic states i.e. ferroelectricity, ferromagnetism and ferroelasticity [1-2]. Multiferroics are used in memory devices, spintronics [3-4] and in many potential applications. It becomes a hot topic of research in recent years. Magnetism appears in the materials which have partially filled d orbital shells whereas ferroelectricity originates from empty d orbital shells. Multiferroics have the ABO_3 perovskite structure.

Brief theory

In this section we will discuss the brief theory of ferroelectricity, ferromagnetism and multiferroism. , since ideal multiferroic materials possess simultaneously both types of ordering. However, antiferromagnetism (AFM) is also considered because $BiFeO_3$ possesses AFM as well as ferroelectricity. The last part is focused on the origin of multiferroism and the properties of multiferroic materials.

2.1.1 Ferroelectricity

Ferroelectricity was discovered in 1921 by Valasek in Rochelle salt. The molecular formula of Rochelle salt is $KNaC_4H_4O_6{\cdot}4H_2O$. Initially this effect was not considered for some time; a few decades ago they approached into a great use [5]. Nowadays, these ferroelectrics are widely used in the memory devices.

It is the phenomenon in which the ferroelectric materials have phase transition above a temperature, this temperature is consider as transition or Curie temperature and above this temperature the ferroelectric materials become paraelectric materials. This phenomenon is known as ferroelectricity. Ferroelectric materials have the spontaneous electric polarization. This polarization is reversible, non-volatile and its direction can be changed by applied field. Polarization (P) is directly proportional to the applied electric field (E) [6]. Most ferroelectric materials are of perovskite structure ABO_3.

The ferroelectric materials have a net dipole moment ($\boldsymbol{\mu}$) that arises from the vector sum of the dipole moments in every unit cell, $\Sigma\boldsymbol{\mu}$. It means that the dipole moment cannot occur in a structure which has centre of symmetry. Therefore, the ferroelectrics should be non-centrosymmetric. It is not only essential along with there must be a local dipole moment (that typically shows a macroscopic polarization but not necessarily if these have domains that cancels completely). It means that central atom should be in the non-equilibrium position [6].

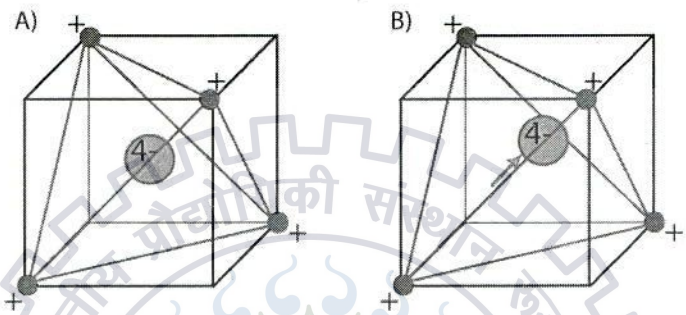

Figure 1.1 Condition for the existence of the dipole moment

General properties of the ferroelectrics:

Polarization

Polarization (**P**) is defined as electric dipole moment per unit volume, and it is related to the dielectric displacement (D) with the linear expression $D = P + \epsilon_0 E$, where P, ϵ_0 and E are polarization, permittivity of free space (equal to 8.854×10^{-12} Coulomb/volt) and applied electric field respectively.

There are four types of polarization:

Electronic: Displacement of the electrons with respect to nucleus.

Ionic: separation of negative and positive ions in crystal.

Orientational: alignment of the permanent dipoles (molecules).

Space-charge: free electrons are present and prevented from moving by the barriers such as the grain boundaries.

Spontaneous polarization

Spontaneous polarization (P_S) is the magnitude of polarization in a single domain of ferroelectric material in absence of external field. It is the fundamental property of all the pyroelectric crystals, but it is reorientationable and reversible in the ferroelectrics only.

Most phases of ferroelectrics arise from non-polar original phase and all the polarization is reorientationable.

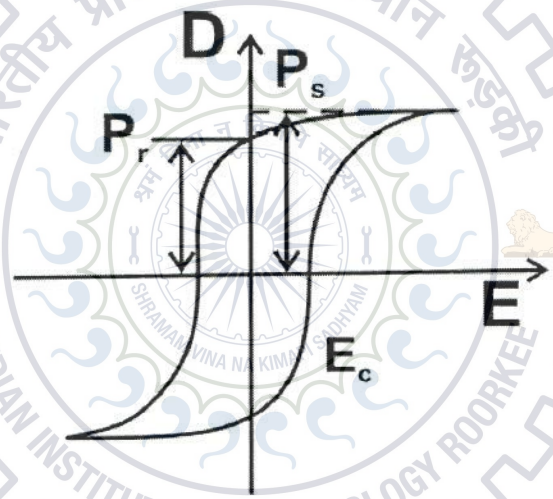

Fig. 1.2 Ferroelectric hysteresis loop (P-E loop)

Hysteresis Loop

By using domain concept, the existence of the hysteresis loop in polarization (P) vs. electric field (E) is described as follows. Considering, initially the overall polarization of a crystal equal to zero, i.e., the vector sum of the dipole moments in the individual domain vanishes. Fig.1.2 shows the hysteresis loop (i.e. P vs. E loop).

When we applied electric field to the crystal, these domains in the crystal with the polarization across the field direction develop at the outgoing of the "antiparallel" domains; therefore, the polarization rises. The crystal becomes a single domain and the polarization saturates whenever all the domains are associated in the same direction of the applied field [7]. With increasing the applied field a further increase in the polarization results from "normal polarization" may effects; the rotation of domain vectors may also be convoluted if the external field does not coexist with any possible direction of the spontaneous polarization. The extrapolation of linear part (saturated value of the polarization) to zero external field as shown in fig. (1.2) that gives the spontaneous polarization Ps (since the relation among electric displacement, electric field and polarization, $D = P + \varepsilon_0 E$), in the above relation, the polarization arises from both the polarization of the material in the presence of a field and from the spontaneous alignment of dipoles in the ferroelectric. The dependence of spontaneous polarization on temperature or on the other external conditions that might be imposed can be measured from the hysteresis loop which is displayed on an oscilloscope screen. When the applied field is reduced for a crystal in Fig. 1.2, the polarization of the crystal also decreases, but there is some remnant polarization (P_r) when the applied field is zero. A hysteresis loop illustrates the coercive field (E_C), the remnant polarization (P_r) and the spontaneous polarization (P_s). Further, to remove remnant polarization (P_r), the polarization must be reversed of the crystal and this occurs when a negative field is applied to the crystal. This field is called the coercive field (E_C) where the polarization is zero [8].

2.1.2 Ferromagnetism

The phenomenon of ferromagnetism was discovered about more than 2000 years ago. Ferromagnetic materials undergo a phase transition from paramagnetic phase (high temperature) to the ferromagnetic phase (low temperature) at a temperature. This temperature is considered as Curie temperature (T_C) [9].

In the ferromagnetic materials, there is a net magnetic moment because of the coupling between the spins in the preferred orientation (remembering this coupling of spins is the quantum

mechanical in the nature, not entirely from the magnetic forces which acting between the neighbouring atoms). Fig. 1.3 shows the different types of magnetic ordering.

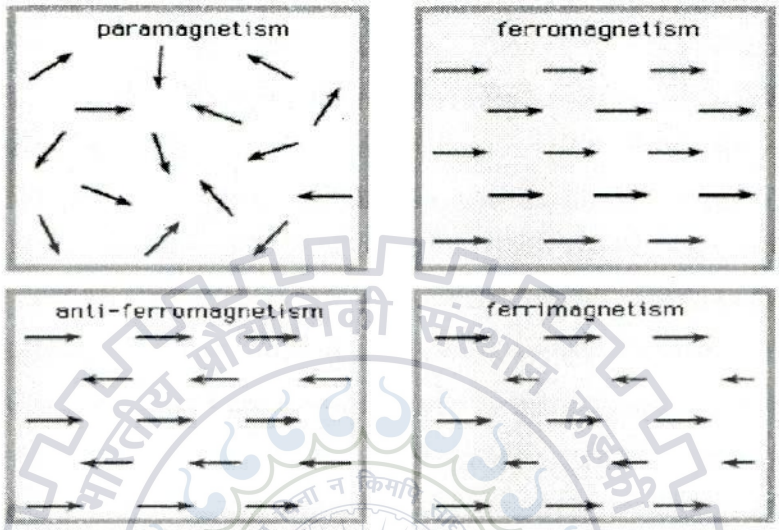

Fig.1.3 Different types of magnetic ordering.

In the paramagnets there is random orientation of the spins when we applied the field spins are oriented in the direction of applied field. When the field is removed, ferromagnetic materials retain the component of the magnetization in the direction of applied field i.e. they are permanently magnetized (they have hysteresis). Also, their susceptibility is independent on the temperature.

Antiferromagnetism

In antiferromagnetic materials, the spins of the electrons give no overall magnetization because the spins are opposite to each other in the crystals. These materials also possess a phase transition from paramagnetic state to the low temperature state with the antiferromagnetic ordering. While in ferrimagnetism, the spins of the electrons give small overall magnetization.

2.1.3 Multiferroism

Multiferroic materials are the materials which exhibit two or more ferroic states (i.e. ferroelectricity, ferromagnetism and ferroelasticity) [1-2]. These materials also known as multifunctional materials. In ferromagnetic materials, the alignment of the electron spins can be switched by the magnetic field; in ferroelectric materials, the polarization can be switched by an electric field and the stress field can switch the strain alignment in ferroelastics. While in multiferroics, polarization can be switched by a magnetic field and magnetization can be switched by an electric field and vice versa. Figure 1.4 shows the interactions in multiferroic materials.

In 1959, Landau and Lifshitz showed the theoretical possibility of the coupling between electric and magnetic ordering in a single material [10]. Such type of materials has magnetization that is controlled via electric field and polarization proportional to the magnetic field. Later, Dzyaloshinskii [11-12] and Astrov observed this type of coupling is known as magnetoelectric effect.

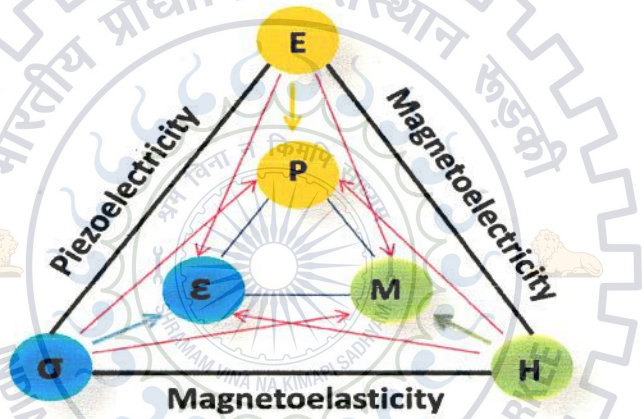

Figure 1.4 Interactions in multiferroic materials.

The next step was to create a novel material that possesses two or more ordering i.e. ferroelectricity and ferromagnetism. This was first achieved by Soviet Scientists. Nevertheless, the study of the multiferroics was stopped soon later due to very few multiferroic materials are the linear magnetoelectrics. Further, increase of interest in the multiferroics begun again around

2003. At present many researcher are working on multiferroics. Nowadays multiferroics are used for potential applications, such as magnetic sensors, transducers, magnetic data storage devices, quantum electro-magnets and spintronics [13-14].

Types of multiferroics

Mainly there are two types of multiferroics. The summary of the pathways to multiferroics including type I and type II and relative materials [10] are given in following table:

	Pathways to	Mechanism for the multiferroism	Examples
Type I	A-site driven	Ferroelectricity arises from A-site (Bi) lone pair and B-site (Fe) cation gives magnetism.	$BiFeO_3$, $BiMnO_3$
	Geometr-ically driven	The system comes to the stable ferroelectric state due to the oxygen rotations and long range dipole- dipole interactions.	$YMnO_3$, $BaNiF_4$
	Charge ordering	Ferroelectricity arises in magnetic materials due to non-centrosymmetric charge ordering	$LuFe_2O_4$
Type II	Magnetic ordering	Formation of symmetry that lowered the magnetic ground state lacking inversion symmetry induced ferroelectricty.	$TbMno_3$, $DyMnO_3$

From the above multiferroic materials bismuth ferrite (BiFeO3) is the only material that shows a microscopic coupling of electric and magnetic ordering at room temperature [15].

2.2 Magnetoelectric Effect

Magnetoelectric effect (ME) is a phenomenon in which the inducing magnetic or electric polarization can be achieved by an applied magnetic (electric) field. This effect may be linear or/and non linear in respect of the external fields. Generally, ME effect depends upon the temperature. This effect is expressed as:

$$P_i = \sum \alpha_{ij} H_j + \sum \beta_{ijk} H_j H_k + \dots$$
$$M_i = \sum \alpha_{ij} E_j + \sum \beta_{ijk} E_j E_k + \dots$$

Here 'P' is the electric polarization, 'M' is the magnetization, 'E' is the applied electric field, 'H' is the magnetic field, and α, β are linear and non linear magnetoelectric susceptibilities respectively. This effect may be found in both single phase and the composites. For example, single phase materials are Cr_2O_3 [16] and multiferroics that show the coupling in electric and magnetic ordering. The composite magnetoelectrics are the combinations of electrostrictive and magnetostrictive materials like piezoelectric and ferromagnetic materials. And the size of this effect is dependent on nanoscopic mechanism. In the single phase, this effect is due to the combination of electric and magnetic ordering as found in some multiferroic materials and in composites this effect originates from the interface effects as the strain. The applications of ME are advanced logic devices, tunable microwave filters and sensitive detection of the magnetic fields.

2.3 Perovskite Structure

A perovskite structure of any material is such type of crystal structure as the calcium titanate with the formula $CaTiO_3$, known as the perovskite structure, or $A^{2+}B^{4+}O_3^{2-}$ [17]. The perovskite name comes from this compound that was discovered by Gustav Rose in 1839, in Ural Mountains of Russia. It was named by L. A. Perovski, a Russian mineralogist. The perovskite structure of crystals was first reported in 1926 by V. M. Goldschmidt. Generally, it has the chemical formula ABO_3, where A and B are the two cations having different size, and O

is anion. Many oxides have the perovskite structure of the formula ABO_3. In an idealized cubic unit cell, the atom A sits at the corner positions i.e. (0, 0, 0) of the cube, the atom B sits at the centre position i.e. (1/2, 1/2, 1/2) and the atoms O sit at the face centered positions i.e. (1/2, 1/2, 1/2).

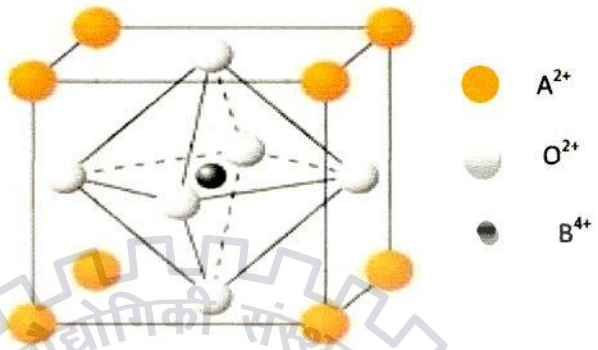

Fig.1.5 Schematic of Perovskite Structure

Figure 1.5 shows the edges for the unit cell in which A at corners, atom B at body centre and the O at faces of the cube.

2.4 Barium Titanate ($BaTiO_3$)

Most of the important ferroelectrics are oxides that possess the well known structure (i.e. perovskite structure). $BaTiO_3$ [18] is one of them which having perovskite structure. Apart from its outstanding properties such as high dielectric constant, piezoelectricity and pyroelectricity, $BaTiO_3$ shows ferroelectricity at the room temperature.This makes $BaTiO_3$ to the essential ferroelectric perovskite material. For $BaTiO_3$, Ti is a 3d transition element and has the d orbital for electrons to form covalent bonds with its neighbors. The radius of Ba^{2+} is about 1.35 A^0 and that of Ti^{4+} ion is about 0.68 A^0. These ions form a nice octahedral cages, with the O^{2-} ions held apart. The structure of $BaTiO_3$ is shown in fig. 1.5, where A stands for Ba^{2+} and B for Ti^{4+}. $BaTiO_3$ is the temperature dependent at certain transition temperatures, the particular structure of the unit cell becomes unstable and must transform to a more stable one. The temperature dependence of $BaTiO_3$ structure is shown in fig. 1.6. Below 120^0C the structure of $BaTiO_3$ changes from cubic to tetragonal phase resulting from the stretching of the cubic unit cells along

one edge, as shown in Figure. In fact, the Ba^{2+} ions shift in the upward direction from the original position in cubic structure; Ti^{4+} ions also shift upward and the O^{2-} ions shift downward to form tetragonal structure. As a result, shifting in ions the centroid of the negative charges does not coincide with the centroid of the positive charges. Therefore, the unit cell becomes permanently polarized and behaves as the permanent dipoles, leading to the spontaneous polarization.

Although $BaTiO_3$ is a high dielectric material with the high values of the piezoelectric and pyroelectric coefficients but hopping of the electrons between Ti^{3+} and Ti^{4+} ions increases the leakage current and also makes it chemically unstable.

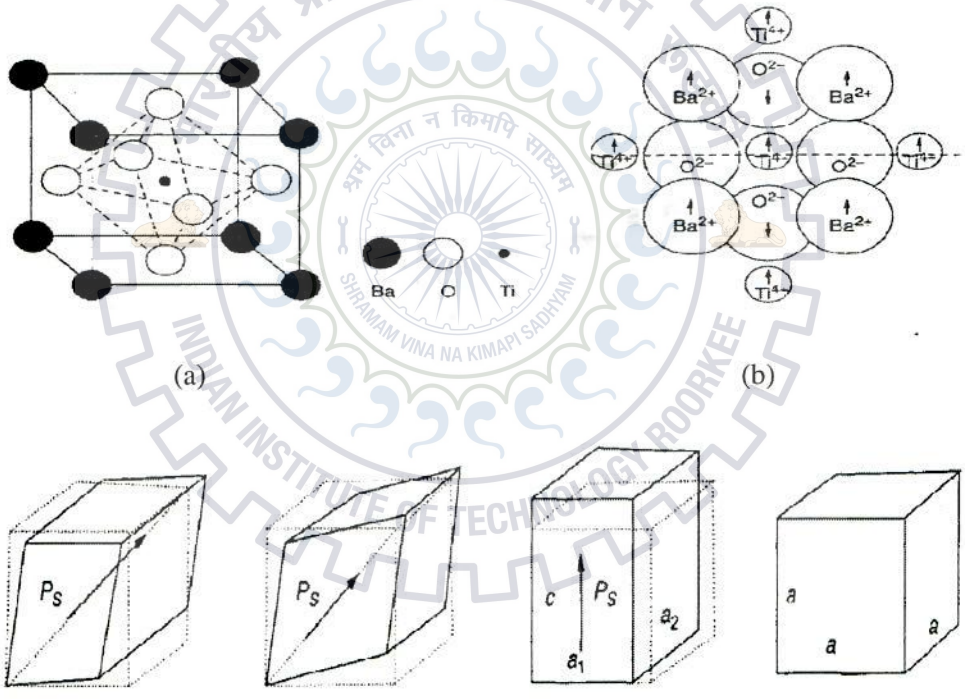

Fig. 1.7 (a) Unit cell of $BaTiO_3$ (b) Ion displacement due to the cubic-tetragonal distortion in $BaTiO_3$ (c) The temperature dependence of $BaTiO_3$ structure .

To reduce the leakage current in $BaTiO_3$ at the cost of the dielectric constant. Usually, for the ABO_3 perovskite structure, by introducing A or/and B sites [19] with the others that enhances the dielectric properties of the given materials. There are two main categories for A and/ or B site substitution of ABO_3 perovskite.

(1) **isovalent substitution**: A or/and B-sites has been substituted with the ions of same type, substitution of this type usually bring curie temperature towards the lower side and lowers the dielectric constant.

(2) **offvalent substitution**: A and/or B-sites has been substituted by ions of opposite type.

The structure of $BaTiO_3$ is the temperature dependent. Above 120^0C, it is cubic and from 120^0C down to ~5^0C, there is a distortion to a tetragonal phase. Further, from 5^0C down to around -90^0C, the structure is orthorhombic and finally at low temperature (below -90^0C) shows rhombohedral, distortion along the body diagonal. These all the structure of $BaTiO_3$ are shown in figure 1.7 (c).

2.5 Bismuth Ferrite ($BiFeO_3$)

Bismuth Ferrite ($BiFeO_3$) is an inorganic chemical compound and a well known multiferroic material with perovskite structure because it shows both ferroic states such as ferroelectricity and magnetism (antiferromagnetism) above the room temperature. It was first incorporated in 1957 by Swars and Royen[20]. It is also denoted as BFO in material science. Numerous studies of multiferroics have been assigned to this compound inspired by the multiferroic properties and magnetoelectric property. The structure of $BiFeO_3$ is rhombohedral that belongs to the R3c space group. $BiFeO_3$ is synthesized in both form i.e. bulk and thin film and both are having G- type antiferromagnetism ordering. Antiferromagnteism Neel temperature (T_N) and ferroelectric Curie temperature (T_C) of BFO are well above the room temperature (approximately T_N ~643K and T_C ~1103K respectively) [21]. For the rhombohedral unit cell, the lattice parametres are a = 5.59 Å and $\alpha = 60.68^0$ [22]. And in such distortion, the symmetry of R3c allows development of the spontaneous polarization 'P_S' through the pseudocubic [111]

direction with the magnitude of 90 - 95 $\mu C/cm^2$ [22]. The structure of the bulk BFO is shown in fig 1.7.

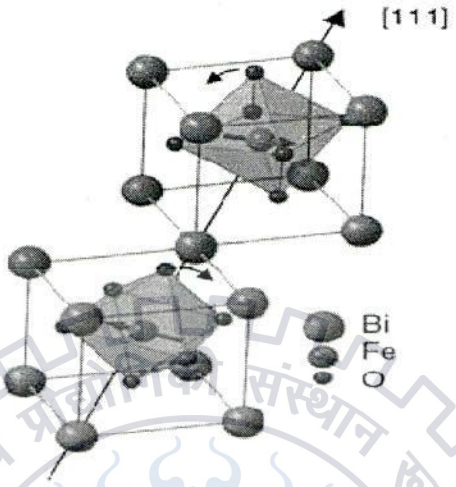

Fig.1.8 The crystal structure of the bulk $BiFeO_3$[23].

The spontaneous magnetetization in the BFO can be caused by substitution of the Fe^{3+} ion by the other transition metal ions or in Bi^{3+} by the other diamagnetic ions, or by the co-substitution at the both Fe^{3+} and Bi^{3+} sites. The ferroelctricity of the BFO is caused by lattice distortion arising from the lone pair of the Bi^{3+}. The large polarization is achieved in $BiFeO_3$ thin films and hetrostructures [24]. The electrical characterization of the bulk BFO has been more difficult due to their lower resistivity. The controversy whether it is antiferroelectric or ferroelctric was finally based on hysterisis loop given by Teague et al., who has performed the experiments at the liquid nitrogen.

Sonsnowka [25] has studied the $BiFeO_3$ magnetic structure and found that spin of each Fe^{3+} ion is surrounded by the six antiparallel spins (spin up) with the nearest iron (Fe) neighbors (spin down), shown in figure 1.9, which is a G-type antiferromagnetism. It means that the magnetic moments of the Fe are paired ferromagnetically in the pseudocubic (111) direction and the antiferromagnetically between the adjacent planes.

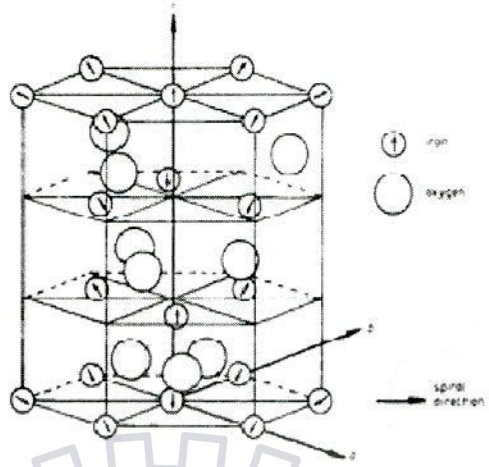

Fig.1.9 A part of $BiFeO_3$ lattice with the iron and the oxygen ions, the arrows show Fe^{3+} moment direction [25].

Figure 1.9 shows a G – type antiferromagnetism in the $BiFeO_3$ with only iron and the oxygen ions. And arrows indicate the moment direction of the Fe^{3+}.

As the bulk BFO is a ferroelectric at room temperature, has spontaneous polarization that is directed along (111) directions of perovskite structure fig. (1.8). The value of spontaneous polarization through the (100) direction is 3.4 $\mu C/cm^2$ and 6.0 $\mu C/cm^2$ [22] through the (111) direction at the 77 K [26], that is smaller than what would be expected for ferroelectric material with such high temperature (T_C).

In the recent times, the BFO has been observed as a predominant material for the progress of the multifunctional devices due to their peculiar optical, ferroelectric, magnetic and piezoelectric properties.These are lead free piezoelectrics and in visible region, they show large flexibility. These qualities make the BFO a specialy applicable in fields of optics, piezoelctrics, ferroelectrics and magnets. In addition, these properties show the cross correlation that expected above the room temperature.

REFERENCES:

[1]. N. A. Spaldin, Science 309, 391 (2005).

[2]. H. Schmid, Ferroelectrics 162, 317 (1994).

[3]. W. Erenstein, N. D. Mathur, and J. F. Scott, Nature 442, 759 (2006).

[4]. M. Fiebig, J. Phys. D: Appl. Phys. 38, R123 (2005).

[5]. See J. Valasek (1920). "Piezoelectric and allied phenomena in Rochelle salt". *Physical Review* **15**: 537. and J. Valasek (1921). "Piezo-Electric and Allied Phenomena in Rochelle Salt". *Physical Review* **17** (4): 475.

[6]. Review article on Ferroelectrics, Piezoelectrics and pyroelectrics.

[7]. D. Jayalakshmi. "Ferroelectric and Thermal Properties of L-Methionine Doped Triglycine Sulphate Crystal", Ferroelectrics, 2006.

[8]. H. V. Keer, Principles of Solid State Physics, Wiley Eastern, New York (1993).

[9]. Review article on ferromagnetic and anti ferromagnetic materials.

[10]. Martin, L.W.. "Multiferroic and magnetoelectric heterostructures", Acta Materialia, 2012.

[11]. I. E. Dzyaloshinskii, Sov. Phys. JETP 10, 628 (1959).

[12]. C. Ederer and C. J. Fennie, J. Phys.: Condens. Matter 20, 434219 (2008).

[13]. W. Erenstein, N. D. Mathur, and J. F. Scott, Nature 442, 759 (2006).

[14]. M. Fiebig, J. Phys. D: Appl. Phys. 38, R123 (2005).

[15]. D. Lebeugle, D. Colson, A. Forget, M. Viret, A. M. Bataille, and A. Gukasov, Phys. Rev. Lett. 100, 227602 (2008).

[16]. C. W. Nan et al., J. App. Phys. 103, 031101 (2008).

[17]. Wenk, Hans-Rudolf; Bulakh, Andrei (2004). Minerals: Their Constitution and Origin.

[18]. M. M. Vijatović, J. D. Bobić, B. D. Stojanović: Review article on Barium Titanate ($BaTiO_3$), **40** (2008) 155-165.

[19]. Chan, N. Y. "Preparation and characterizations of $Ba(Zr,Ti)O_3/(Ba,Sr)TiO_3$ heterostructures grown on $(LaAlO_3)0.3$-$(Sr_2AlTaO_6)0.35$ single crystal substrates by pulsed laser deposition", Thin Solid Films, 2010, 1001.

[20]. A. P. Pyatakov, A. K. Zvezdin., "Magnetoelectric and multiferroic media", Physics-Uspekhi 55, 557 (2012)

[21]. Spaldin, Nicola A.; Cheong, Sang-Wook, Ramesh, Ramamoorthy (1 January 2010), Multiferroics: Past, present, and future, Physics Today **63** (10): 38.

[22]. Alessandro Alan Porporati. "Raman tensor elements for multiferroic BiFeO3 with rhombohedral *R3c* symmetry", Journal of Raman Spectroscopy, 2009.

[23]. Axel Lubk, S. Gemming, and N. A. Spaldin, Phys. Rev. B Vol. **80**, 104110 (2009).

[24]. Seva (Vsevolod) V. Khikhlovskyi, The renaissance of multiferroics: bismuth ferrite (BiFeO3) – a candidate multiferroic material in nanoscience, 2010.

[25]. I. Sosnowska et al., J. Phys. C. **15**, 4835 (1982).

[26]. Teague, Gerson and James, Solid State Commun. **8**, 1073 (1963).

CHAPTER - 3 SYNTHESIS AND CHARACTERIZATION TECHNIQUES

3.1 Solid State Reaction Method

Many methods are used to make materials but solid state reaction method is a popular and widely used method. It has many advantages over other methods like no required of precursor, simply used at room temperature and no requirement of purification [1].

3.2 Samples Preparation

Solid state or "*shake and bake*" reaction method is used to make pellets of (1-x) $BiFeO_3$-x $BaTiO_3$ composites at different compositions (x=0, 0.1, 0.3, 0.5, 0.7 and 1.0) [2]. This method is probably more traditional and by this route we have been prepared an extremely large number of the single-phase perovskite materials with high quality that can be used in many applications. The following sections present the synthesis procedure of ceramic pellets used in this thesis.

3.2.1 Synthesis of $BiFeO_3$ (BFO)

Stoichiometric $BiFeO_3$ (BFO) pellet was synthesized by the solid state reaction method (SSR) [3]. Starting raw materials used with high purity bismuth oxide (Bi_2O_3) and Iron oxide (Fe_2O_3). These precursors were mixed in requisite ratio and then grinded for 10-12 hrs. After this we mix binder polyvinyl alcohol (PVA) and again grinded for 3 hrs. After that, by mixing the mixture properly and pressed in the form of pellets. The pellet then sintered at 870°C for 5 min with the heating rate of 10^0C and then rapidly quenched in liquid N_2.

Synthesis of BFO by Solid State Reaction Method

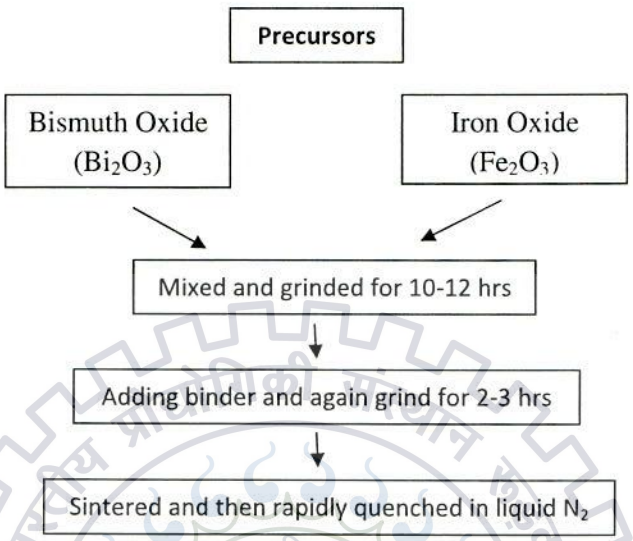

3.2.2 Synthesis of (1-x) $BiFeO_3$ (BFO) – x$BaTiO_3$ (BTO) composites

The pellets of stoichiometric (1-x) $BiFeO_3$ – x$BaTiO_3$ composites at different values of x (i.e. x = 0, 0.1, 0.3, 0.5, 0.7 and 1.0) were prepared by the solid state reaction method. At x=0, (i.e. pure BFO), we discussed the synthesis of BFO is already. At x= 0.1, 0.3, 0.5 and 0.7, the starting materials for these samples are bismuth oxide (Bi_2O_3), Iron oxide (Fe_2O_3), barium carbonate ($BaCO_3$) and titania (TiO_2). These precursors were mixed in requisite ratio and then grinded for 10-12 hrs. Calcinations were carried out at 750^0C for 1 hr for all samples. After this binder polyvinyl alcohol (PVA) is mixed and again grinded for 3 hrs. After mixing of these mixtures properly, we pressed the mixtures into the pellets. The pellets then sintered at 980^oC, 980^0C, 1020^0C and 1040^0C (at x = 0.1, 0.3, 0.5 and 0.7) for 5 min with the heating rate of 10^0C respectively and then rapidly quenched in liquid N_2.

CHAPTER - 3 SYNTHESIS AND CHARACTERIZATION TECHNIQUES

Synthesis of (1-x) BFO – x BTO composites by Solid State Reaction Method

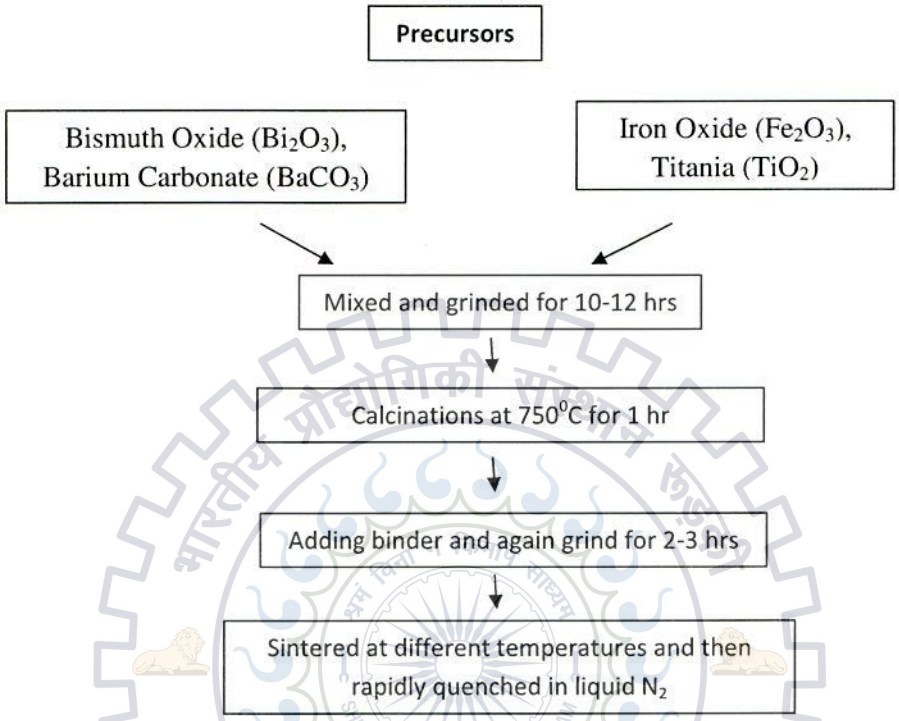

3.2.3 Synthesis of $BaTiO_3$ (BTO)

Stoichiometric $BaTiO_3$ (BTO) pellet was prepared by the solid state reaction method [3]. Starting raw materials for this occured high purity barium carbonate ($BaCO_3$) and titania (TiO_2). These precursors were mixed in requisite ratio and then grinded for 10-12 hrs. Calcination was carried out at 1150^{0}C for 4 hr. After this we mix binder polyvinyl alcohol (PVA) and again grinded for 2-3 hrs. The mixture was mixed properly and pressed into the pellets. The sintering of the pellet is done at 1300^{o}C for 4 hrs with the heating rate of 10^{0}C.

Synthesis of BTO by Solid State Reaction Method

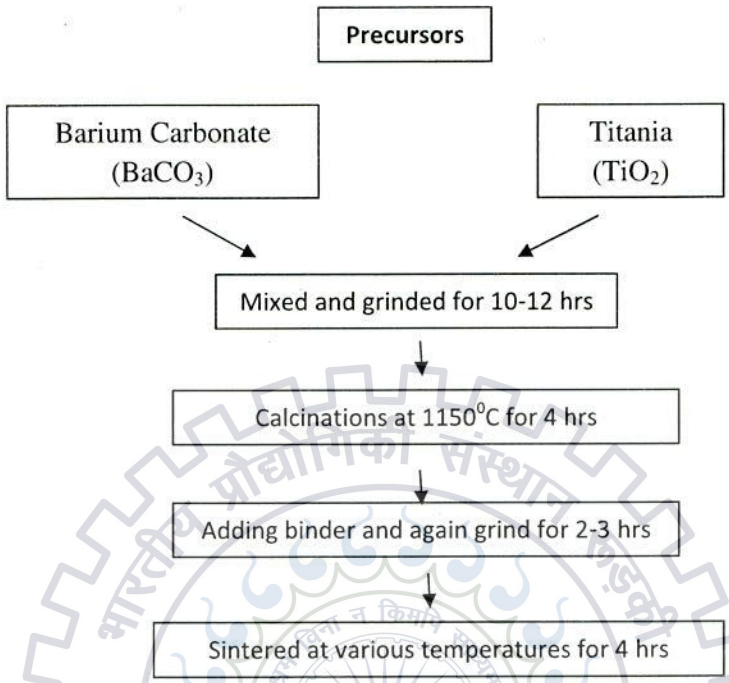

3.3 The Structural Characterization Techniques

3.3.1 X-Ray Diffraction (XRD)

X-ray diffraction method is primarily used for the phase identification of a crystalline material. It is most widely used in the crystal structure determination, including lattice constants, crystallite size, phase analysis, crystal defects, stress etc. X-ray data provides information regarding the crystalline structures of different materials in bulk, powder and thin film forms. Such data can be used to determine the relative atomic positions atoms of simple and complex materials.

Fig 3.1 shows the basic principle of X-ray diffraction. A parallel beam of X-rays strikes the crystal where the atoms are placed on parallel planes which are separated by a distance'd' (interplanar spacing). The parallel X-ray beams on the left impinge onto the planes at an angle θ and the atoms scatter the X-ray beams in all directions [4]. The interaction of the incident rays

with the sample produces constructive interference and mathematically this is expressed by Bragg's law

$$2dsin\theta = n\lambda \quad (3.1)$$

where,'d' is the spacing between two adjacent atomic planes, 'θ' is the angle between the atomic plane and X-ray, 'n' is the order of diffraction maximum, and λ is the wavelength of the X-rays [5].

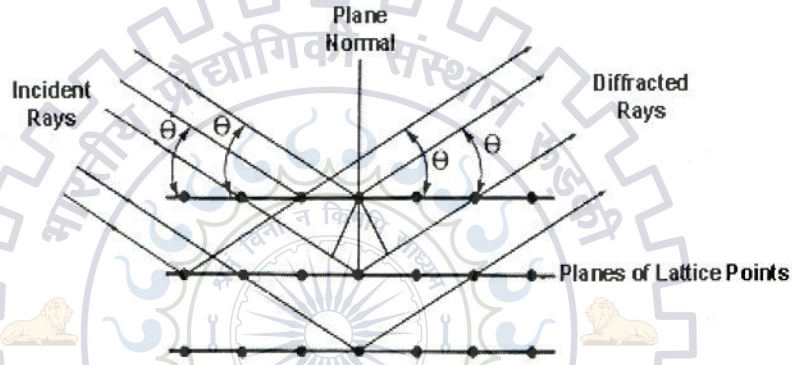

Fig. 3.1 Diffraction of X-rays by crystal planes

The XRD pattern can also provide the information about the material's microstructures such as crystallite size. The crystallite size of a crystallized material is usually related with the full width half maximum (FWHM, 'β') of an X-ray diffraction peak (Fig.3.2). The peak width (β) is measured from the diffraction peak where its intensity is at half of its maximum intensity. The measured FWHM can be mathematically converted into the crystallite size of nanostructures by using the **'Scherrer's Equation'** [6].

The Scherrer equation can be expressed in the following form,

$$D = \frac{0.9\lambda}{\beta cos\theta} \quad (3.2)$$

Where D is the average crystallite size, λ is the wavelength of the incoming X-ray beam (Cu-Kα radiation, 1.5402 Å), β is the FWHM of diffraction peak in radius, is the position of the diffraction peak.

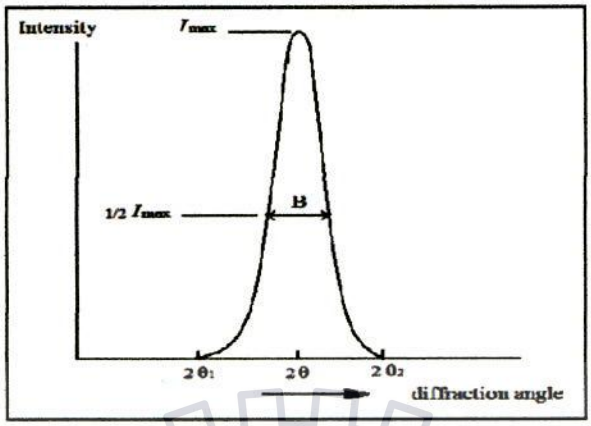

Fig. 3.2 Effect of grain size on X-ray diffraction peak

The X-ray diffractometer in the Nano Science laboratory (IIC, IIT Roorkee) is shown in figure (3.3),

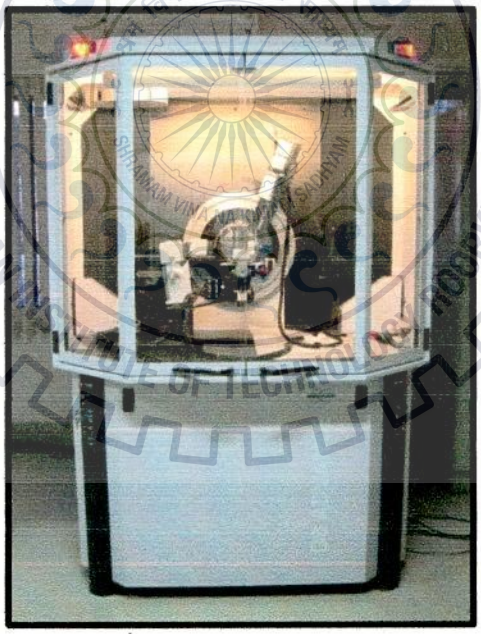

Fig. 3.3 X-ray diffractometer (Bruker AXS, D8 Advance), IIC, IIT Roorkee.

The X-ray diffraction pattern can also be used to calculate the lattice parameters of the crystal structure. For example, the lattice parameters of the rhombohedral structure (a=b=c, $\alpha=\beta=\gamma\neq90^{o}$), for the tetragonal structure (a=b $\neq$c, $\alpha=\beta=\gamma=90^{o}$) and for cubic structure (a=b=c, $\alpha=\beta=\gamma=90^{o}$) can be calculated from the following equations [5].

$$\frac{1}{d^2}=\frac{(h^2+k^2+l^2)sin^2\propto+2(hk+kl+hl)(cos^2\propto-cos\propto)}{a^2(1-3cos^2\propto+2cos^3\propto)} \quad 3.3$$

And

$$\frac{1}{d^2}=\frac{h^2+k^2}{a^2}+\frac{l^2}{c^2} \quad 3.4$$

$$\frac{1}{d^2}=\frac{h^2+k^2+l^2}{a^2} \quad 3.5$$

3.3.2 Field Emission Scanning Electron Microscopy (FE-SEM)

A Scanning Electron Microscope (SEM) is such type of electron microscope which scans the sample along with a focused electron beam and produce images of the sample. These electrons contact with the atoms in sample that produces different signals, can be observed and that carry information regarding the surface topography of the sample and composition. The SEM can attain resolution superior than 1 nm and specimens can be observed in the low vacuum, in the high vacuum and also in the wet conditions [7].

In conventional SEM, Tungsten is used as filament because it has low vapor pressure and high melting point [8, 9]. On the other hand, in Field Emission Scanning Electron Microscope (FE-SEM) electrons are emitted via field emission (FE) by applying high voltage. FE-SEM provides 2 nm resolutions which is 3 to 6 times better than the conventional SEM, and minimizes sample charging and damage. Fig. 3.4 shows a schematic diagram of the field emission scanning electron microscope. The beam of electrons produces by an electron gun, typically having energy

ranging from a few hundred eV to 50 keV. A scan generator produces a varying voltage, by which coils are energized and it creates a magnetic field, which diverts the electron beam back and forth in a controlled design called a raster scan (point by point scanning) over a rectangular region of the sample surface [7, 10].

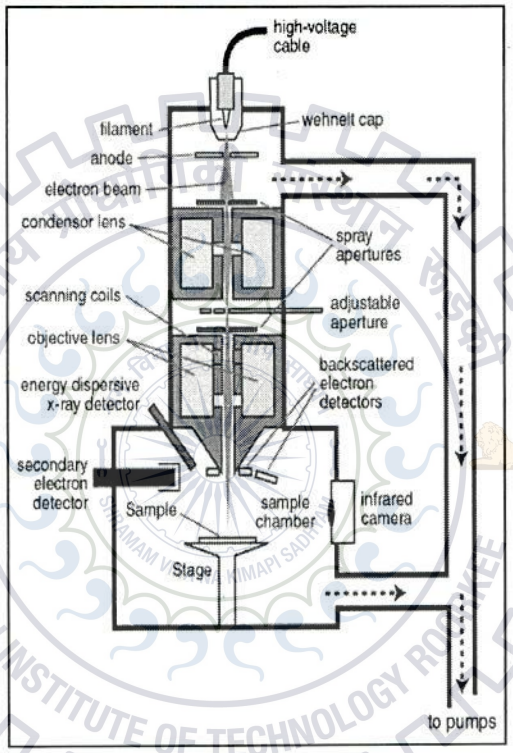

Fig. 3.4 Schematic diagram of the Field Emission Scanning Electron Microscope

When the beam of incident electrons strikes the surface of a sample, it produces variety of signals such as:

Signal		Information
(i) Secondary electrons	:	Surface Morphology and Topography of the samples
(ii) Backscattered electrons	:	Composition in multiphase samples

(iii) Diffracted backscattered electrons : Orientation of the grains

(iv) Photons or Characteristic X-rays : Identification of material and quantitative or semi-quantitative analysis

Some other signals are also generated during the interaction such as Bremsstrahlung X-rays, Auger electrons, visible light (cathodoluminescence), specimen current and heat. The interaction of the electron beam with the sample is shown in figure (3.5),

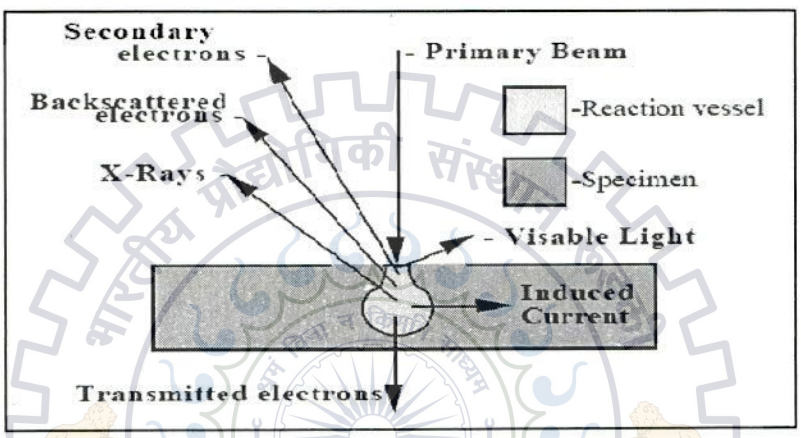

Fig. 3.5 Interaction between electron beam and sample

The reflected beam of electrons from the sample by an elastic scattering considered as Back-scattered electrons (BSE) and the intensity of these electrons is strongly associated to the atomic number (Z) of the sample. The BSE images can yield information over the distribution of various elements present in the sample. When an electron beam interacts with the inner shell, an electron removes that releases characteristic X-rays which fill the shell and also release some energy. And these X-rays are utilized to recognize the composition and to measure the affluence of the elements in the specimen [7, 11].

Sample Preparation for FE-SEM

All the samples should be of a proper size that fit properly into specimen chamber and gradually mounted on a holder, which is known as a specimen stub.

For the conventional image in the SEM, the specimens should be conductive at the minimum at the surface and also electrically grounded to stop the gathering of electrostatic charges at the surface. The metal targets need little special arrangement for the SEM besides cleaning and the mounting on a stub. When a non-conducting sample is analyzed, a negative charge built up gradually on the area, where bombardment of electrons occurs.

Therefore, these specimens are coated by an ultrathin coating for the conducting materials; the deposition is taken either by the low-vacuum sputter coating or by the high-vacuum evaporation on the sample.

FE-SEM Set-up

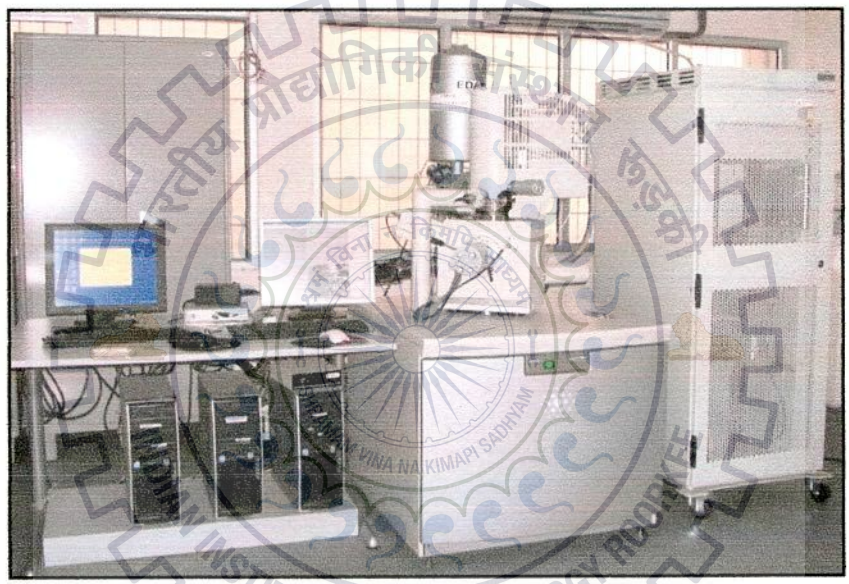

Fig. 3.6 Field Emission Scanning Electron Microscope (FEI, Quanta 200F) at IIC

3.4 Dielectric Measurement

The dielectric properties of the sample are measured using Cryo Chamber and Impedance Analyzer, shown in figure 3.7 (a). For dielectric measurements the samples were prepared by electroding with the silver paste. The frequency range for this was varied from 100 Hz to 1 MHz. The dielectric behavior has also been studied as a function of temperature. With this

experimental setup we can measure the variation in dielectric constant with temperature ranging from 50 K to 450 K. Also, we can also measure the dielectric loss vs. temperature [12, 13].

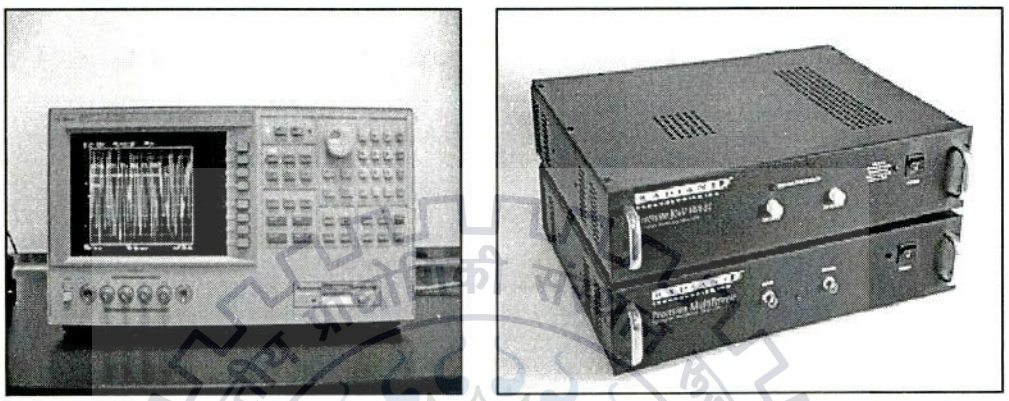

(a) (b)

Fig. 3.7 (a) Agilent Impedance Analyzer, (b) Radiant Ferroelectric Test System

3.5 Ferroelectric Measurement

The ferroelectric properties that are polarization (P) vs. electric field (e) loop, also called hysteresis loop, at room temperature for all samples were recorded by using precision premier II, which is a standard ferroelectric testing machine (Radiant Technology), shown in figure 3.7 (b). With this experimental setup we can measure the electric polarization vs. applied electric field, leakage current vs. frequency and leakage current vs. time. From the P-E hysteresis loop we can also obtain the remnant polarization (P_r), saturation polarization (P_s) etc. and find whether the sample is soft or hard electric. The ferroelectric measurement is based on the principal of the Sawyer- Tower circuit. The schematic diagram of this is shown in figure 3.8. In this circuit, step voltage V is applied to the pair of electrodes on surfaces of a sample capacitor (C_X) with the thickness d. This is then plotted on horizontal x- axis, that is proportional to the applied field, E=V/d, across the sample [14, 15].

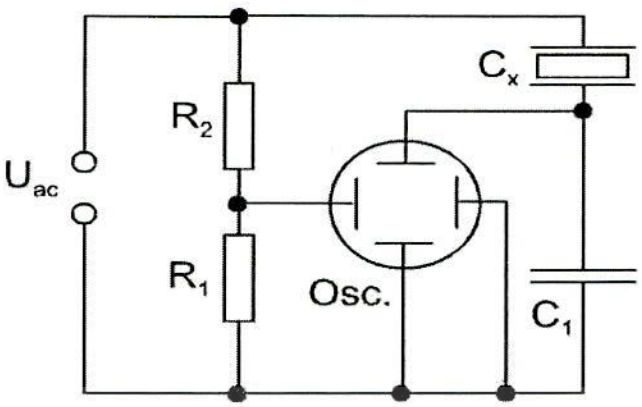

Fig. 3.8 Schematic of Sawyer – Tower circuit for the ferroelectric measurement.

The sample is connected in series with parallel RC circuit; the voltage is measured across the reference capacitor (C_1). Because two capacitors are connected in the series, so the charge on both capacitors must be same. Once charge on the sample is known, polarization can be determined by using the relation.

$$P = Q/A$$

Where Q is the charge on the electrodes and A is the area of the electrodes.

3.6 Differential Thermal Analysis

The differential thermal analysis (or DTA) is a technique that is similar to differential scanning calorimetry (or DSC), used to study the temperature difference between the sample material and an inert reference, that undergo identical thermal cycles [16]. This difference in the temperature is then plotted with time or with the temperature, which is called DTA curve or thermogram. The change in the sample can be detected comparative to the inert reference, either exothermic or the endothermic. It shows at which a material reacts and if the change in heat is positive or the negative. It is more difficult to determine with the DTA measurements, which

kind of reaction is detected. It is a quick method that does not demand complicated instruments [17]. The schematic diagram of DTA is shown in figure 3.9 [18].

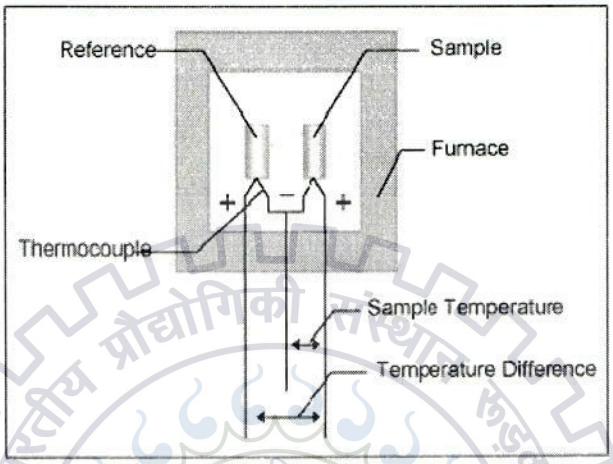

Fig. 3.9 Schematic diagram of the DTA

Principle of DTA

Both reference and the sample are situated symmetrically in the furnace. The furnace is controlled with the temperature program, and this temperature of the reference and the sample are changed. Throughout this process, a differential thermocouple is set up which detect the difference in the temperature between the reference and the sample. The sample temperature is also detected on the sample side from the thermocouple. Fig. 3.10 (a) shows the change in the temperature of the furnace, the sample and the reference with the time, and the fig. 3.10 (b) shows change in the temperature difference 'ΔT' with the time that detected by the differential thermocouple. The ΔT signal is referred as DTA signal.

When furnace starts heating, the sample and the reference begin heating with the slight delay, which depends on their heat capacity.

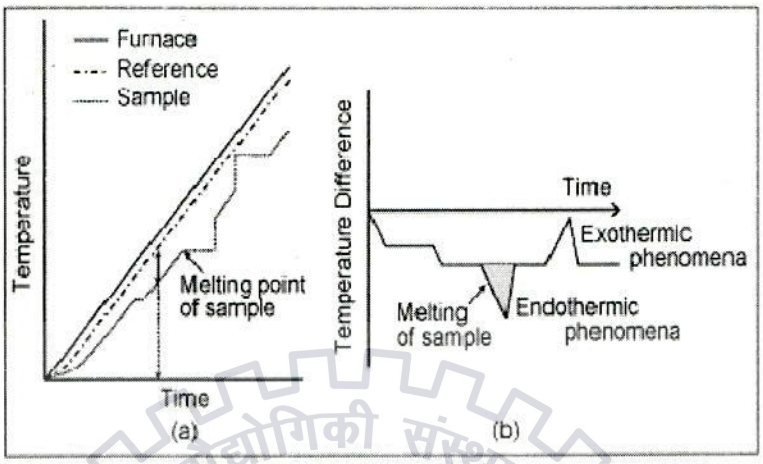

Fig.3.10 Measurement principles of the DTA

After heating begins the ΔT changes till the steady state is reached and after achieving stability, it reaches a set amount adaptable with the difference in the heat capacity between the reference and the sample. This static signal is called the baseline. When temperature increases and the melting arise in the sample, for example, shown in fig 3.10 (a), the temperature rise stops and ΔT increase.

When the melting stops, the temperature curve quickly returns to the baseline. At this point, ΔT signal reaches to the peak which is shown in fig.3.10 (b). From this we can observed the transition temperature of the sample and reaction temperature from ΔT signal. In fig. 3.10 (b), the temperature differences due to the exothermic change is given as positive direction and due to the endothermic change is given as a negative direction [18].

Applications of DTA

1. To study the phase transitions and to construct the diagrams.
2. To find the change in the enthalpy (ΔH).

REFERENCES:

[1]. K.R. Kambale et al. / Ceramics International 38 (2012) 1585-1589.

[2]. Gotardo et al. J. Appl. Phys. 112, 104112 (2012)

[3]. Cai, et al. "Dielectric properties and microstructure of Mg doped barium titanate ceramics", Advances in Applied Ceramics, 2011.

[4]. Kittel, Introduction to Solid State Physics.

[5]. Cullity *et al.*, X-ray Diffraction, 2001.

[6]. Wee, et al. "From Atoms and Molecules to Nanoscale Materials", Science at the Nanoscale an Introductory Textbook, 2009.

[7]. Intro to Field Emission, Field Emission / Ion Microscopy Laboratory, Purdue University, Dept. of Physics. Retrieved 2007-05-10.

[8]. Stranks, D. R.; M. L. Heffernan, K. C. Lee Dow, P. T. McTigue, G. R. A. Withers (1970). *Chemistry: A structural view*. Carlton, Victoria: Melbourne University Press.

[9]. Iafisco, Michele 1980(Roveri, Norberto). "Interaction between biomimetic inorganic materials and biomolecules: towards nanotechnological applications ", Alma Mater Studiorum - Università di Bologna, 2011.

[10]. L. Reimer, G. Pfefferkorn: Raster elektronen mikroskopie (Scanning electron microscopy); Publishing house: Springer-Verlag, Berlin 1977

[11]. Flegler, Heckman, Klomparens: Elektronen mikroskopie (Electron microscopy); Publishing house: Spektrum Akademischer Verlag, Heidelberg 1995.

[12]. Giurgiutiu, V.; Xu, B. (2003) "CEMIA – Compact Electromechanical Impedance Analyzer for Structural Health Monitoring", USC-IPMO, Disclosure ID No. 00407 of 09/28/2003

[13]. Agilent Technologies (2003), Impedance Measurement Handbook (2nd Edition), Agilent Technologies Co. Ltd., Dec 2003.

[14]. M. Dawber, I. Farnan and JF Scott, "A classroom experiment to Demonstrate ferroelectric hysteresis", *American Journal of Physics,* vol. 71, 2003, p. 819.

[15]. Rabe *et al.* (2007).

[16]. Bhadeshia H.K.D.H. "Thermal analyses techniques. Differential thermal analysis", University of Cambridge, Material Science and Metallurgy, 2002.

[17]. P. Gabbott, Ed., *Principles and Applications of Thermal Analysis*, Blackwell, 2008.

[18]. Hitachi High- Tech Science Corporation 2003, 2014 .

4.1 Characterizations of the $BaTiO_3$ ceramic

4.1.1 Structural Studies by XRD

An X-ray diffractometer with the Cu K_α target of wavelength (λ = 1.5406 Å) is used for the structural analysis of the $BaTiO_3$ samples by varying the diffraction angle ranging from 10^0 to 80^0. Following figures show the XRD patterns for the different $BaTiO_3$ pellets, sintered at 1100^0C, 1200^0C and 1300^0C. The pellets are optimized at the above sintering temperatures. These optimized temperatures for the synthesis of $BaTiO_3$ are determined by analyzing these XRD patterns. Formation of the $BaTiO_3$ was confirmed with the JCPDS database. The crystalline $BaTiO_3$ is formed at these sintering temperatures. The XRD peaks confirm the single perovskite phase at these sintering temperatures.

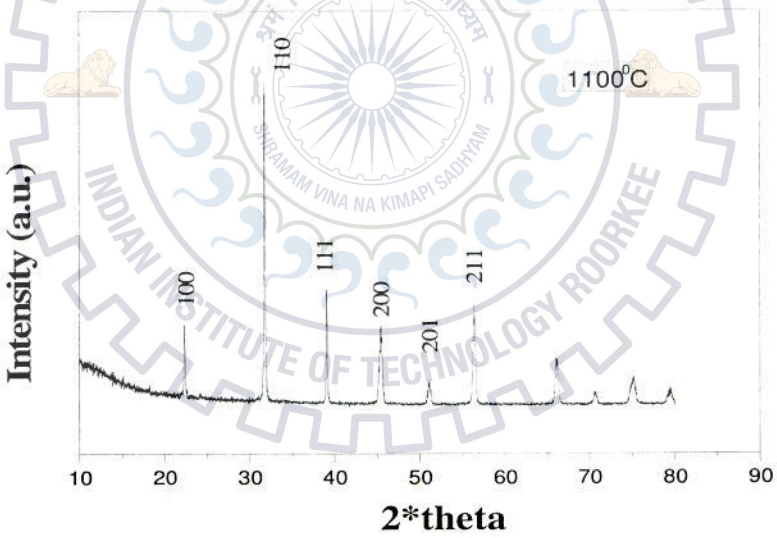

Fig.4.1 XRD pattern of the $BaTiO_3$ sintered at 1100^0C.

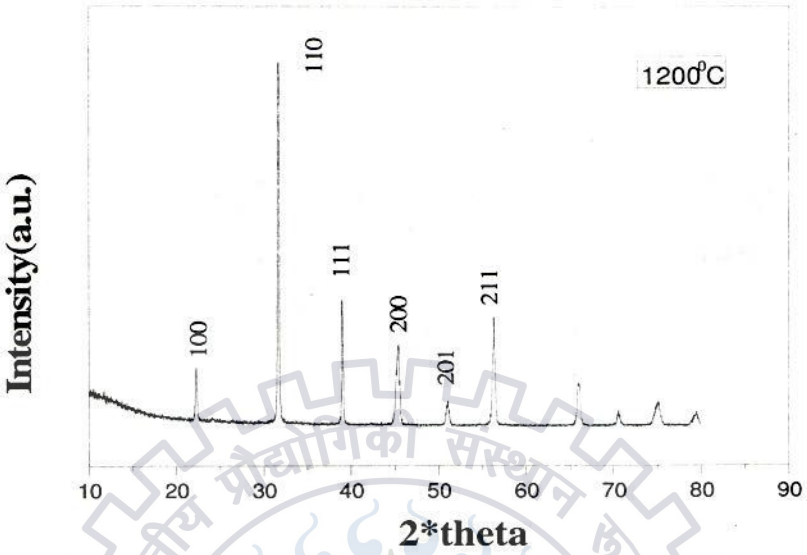

Fig.4.2 XRD pattern of the $BaTiO_3$ sintered at 1200^0C.

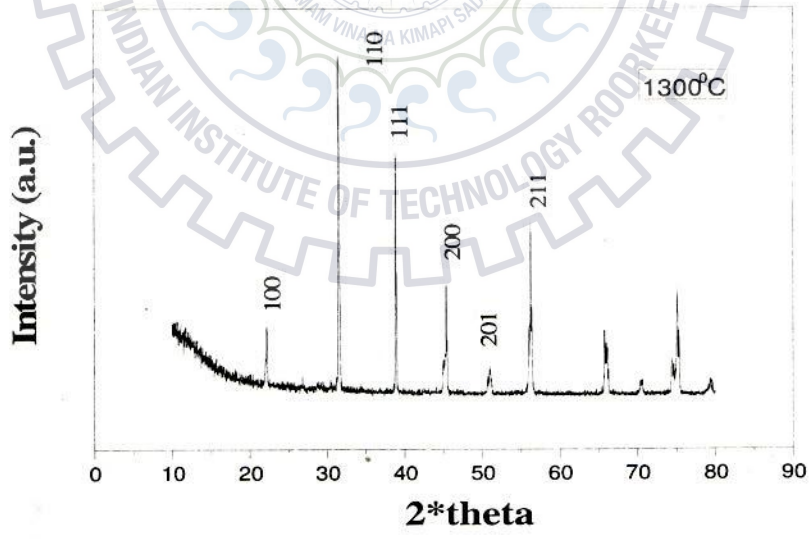

Fig.4.3 XRD pattern of the $BaTiO_3$ sintered at 1300^0C.

Above all XRD patterns of $BaTiO_3$ sintered at different temperatures i.e. 1100^0C, 1200^0C and 1300^0C show pure crystalline phase without any impurities of the secondary phase. By the XRD lattice parameters and crystallite sizes are to be calculated, which are given in the following tables. The calculated values are the nearly same as the theoretical values and the distortion ratio (c/a ratio) is above the one for all the samples [1]. From XRD, it is confirmed that the structure of all $BaTiO_3$ samples is tetragonal [2]. The standard lattice parameters are a = 3.9998 Å and c = 4.018 Å.

The lattice parameters are calculated by the following formula

$$\frac{1}{d^2} = \frac{h^2 + k^2}{a^2} + \frac{l^2}{c^2}$$

And crystallite size (D) is obtained by using

$$D = \frac{0.9\lambda}{\beta cos\theta}$$

Where, β is F.W.H.M. and calculated from the relation:

$$\beta = \frac{\theta_1 - \theta_2}{2}$$

Table 1. Lattice parameters calculated at various sintering temperature

Samples	Lattice Constants (Å)		c/a ratio
	a	c	
BTO 1100	3.9794	4.000	1.0052
BTO 1200	3.9840	4.016	1.0080
BTO 1300	4.0080	4.032	1.0060

From the table 1, it is clear that the standard lattice parameters are in the excellent agreement with the calculated lattice parameters. Hence, these results confirm the formation of the tetragonal $BaTiO_3$ for all samples.

Table 2. Crystallite Sizes calculated at various sintering temperature

Samples	Crystallite Size (nm)
BTO 1100	45
BTO 1200	65
BTO 1300	82

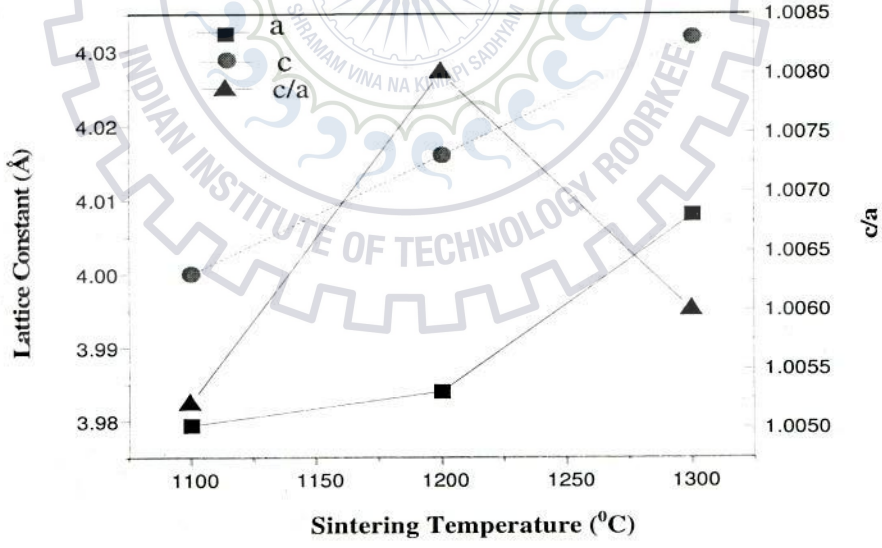

Fig.4.4 Dependence of the lattice constants (a and c), and the c/a ratio (i.e. on right hand side) on the sintering temperature.

From XRD, it is observed that the lattice parameters and the crystallite size of $BaTiO_3$ increase as the sintering temperature increases. These parameters increase due to the unit cell expansion as sintering temperature increases. Figure 4.4 shows the dependence of the lattice constants and c/a ratio on the sintering temperature at the room temperature. From table (1), it is also clear that the distortion ratio (c/a ratio) first increases that is for 1100^0 C and 1200^0C and then decreases for 1300^0C. This means that a strong tetragonal structure at 1200^0C and above 1300^0C it can become a cubic structure since the c/a ratio approaches to 1. From table (2), it is found that the particle size also increases as the sintering temperature increases.

4.1.2 Surface Morphology Analysis

The Surface morphology of the $BaTiO_3$ samples was investigated by a Field Effect Scanning Electron Microscopy (FESEM), and the compositions were determined by EDAX (Energy Dispersive Analysis of the X-rays). The beam of electrons of energy about 15 keV is incident on the samples. Then the resulting X-rays give the information about the surface and the compositions of the specific part under scan.

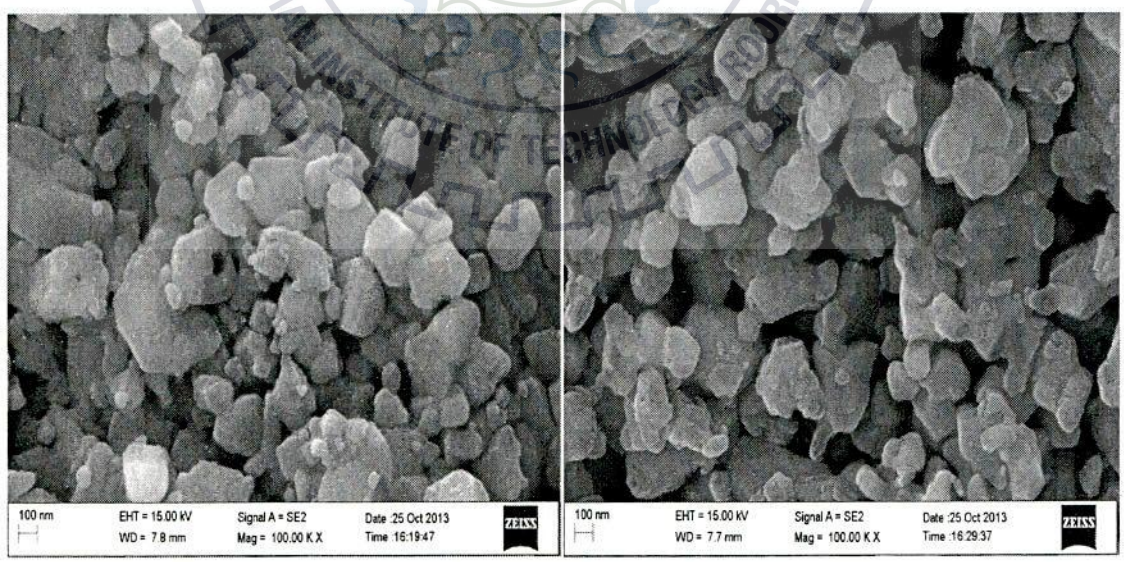

(a) (b)

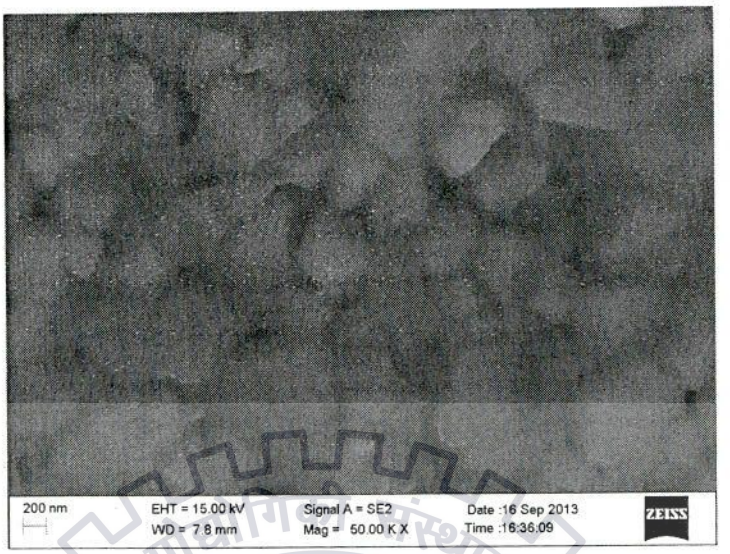

(c)

Fig.4.5 SEM micrographs of $BaTiO_3$ sintered at (a) 1100^0C, (b) 1200^0C, and (c) 1300^0C

From the micrographs, microstructure properties such as grain size, porosity, grain distribution, interfaces and presence of the different phases can be measured.

From figure (4.5), it can be observed that the $BaTiO_3$ has spherical morphology sintered at different temperatures. It is also noticed that the average grain size grows as the sintering temperature increases; this is known as the grain growth. The term grain growth is commonly used in the metallurgy but also used in the ceramics and minerals [3]. This occurs because the grain boundaries have higher energy in comparison of a perfect lattice, so there is a force (called driving force) that reduces the area of the grain boundaries, hence increasing the grain size.

Table 3. Average grain size calculated at different sintering temperatures

Samples	Average grain size (nm)
BTO 1100	360
BTO 1200	450
BTO 1300	570

From the XRD, it is also observed that the density increases, structure is more uniform, more homogeneity and pore free structure as sintering temperature increases. The values of average grain size are calculated for different sintering temperatures are shown in table 3.

4.1.3 Dielectric Properties

Dielectric measurements of the $BaTiO_3$ samples sintered at different temperature were carried out by the impedance analyzer with respects to the temperature at frequency 1 MHz [4]. Fig. 4.6 displays the dependence of the dielectric constant with the temperature. From figure, it is clear that the sintered $BaTiO_3$ samples posses the high relative permittivity at room temperature.

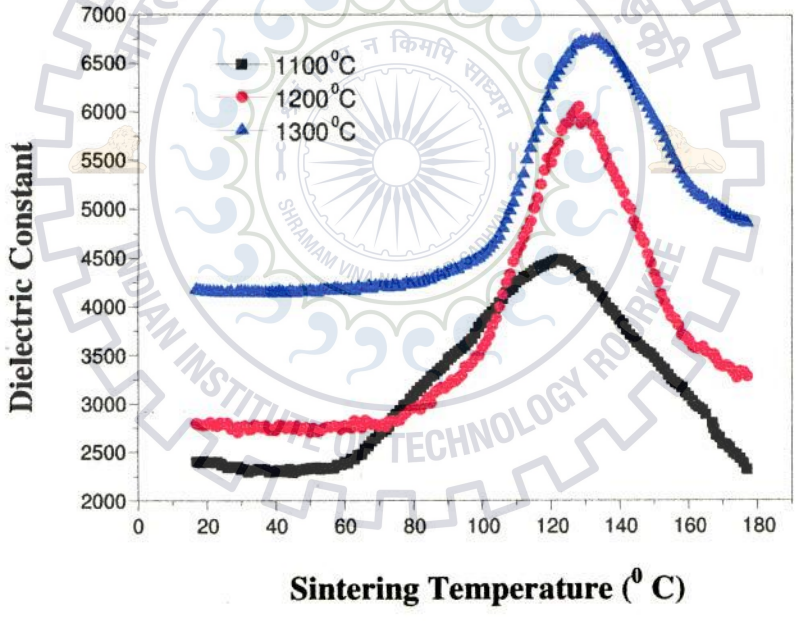

Fig.4.6 Dependence of the dielectric constant with temperature at various sintering temperature.

From figure (4.6), it is clear that the dielectric constant is increasing as the temperature increases. The dielectric constant is found maximum for $BaTiO_3$ sample sintered at 1300^0C.

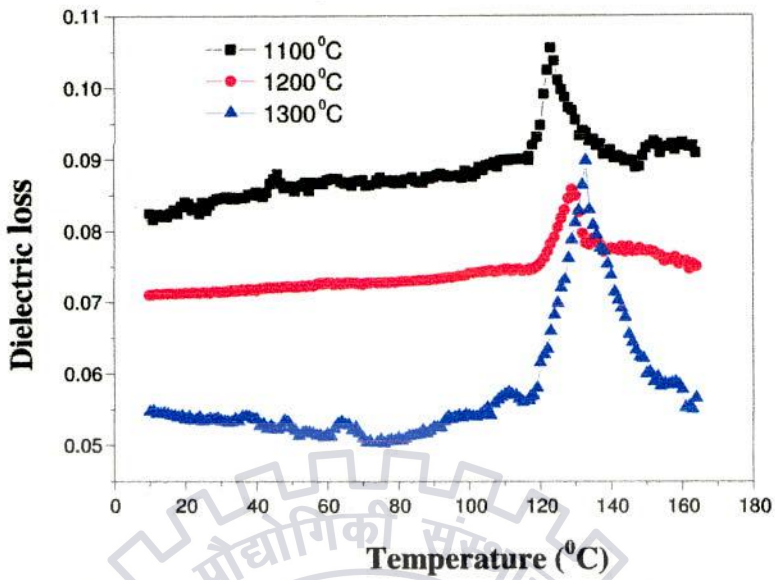

Fig.4.7 Dependence of the dielectric loss with temperature at different sintering temperature.

The phase transition temperature is different for different samples. Curie temperature (T_C) increases with increase in the sintering temperature because the internal stress can shift it to the higher temperature with the increased grain size.

The values of dielectric constant 'ε_r' and the dielectric loss 'tanδ' at room temperature (RT) and Curie temperature (T_C) are given in table.4 [5, 6]. Figure 4.7 shows the dependence of dielectric loss versus temperature at 1100^{0}C, 1200^{0}C and 1300^{0}C sintering temperature. From figure (4.7), it is also observed that the dielectric loss is low for $BaTiO_3$ sintered at 1300^{0}C. The value of dielectric constant is much higher and the value of dielectric loss is much low than the reported [7]. The higher value of the ε_r of BTO samples that found in our case is assigned to uniform and the dense surface microstructure, which show better crystallinity and higher density than the earlier reports on the BTO [7-9]. And the lower value of the tanδ indicates that the synthesize sample was almost impurity/ defect free.

Table 4. The values of ε_r and tanδ at RT and T_C

Samples	T_C	Dielectric Constant		Dielectric Loss	
		At RT	At T_C	At RT	At TC
BTO 1100	123	2500	4500	0.082	0.105
BTO 1200	127	2800	6000	0.07	0.08
BTO 1300	132	4200	6800	0.052	0.082

It is observed that the value of ε_r is much high and tanδ is low of BTO ceramic sintered at 1300^0C. This shows that the BTO sample is much useful sintered at 1300^0C than the other sample sintered at 1100^0C and 1200^0C.

4.1.4 Ferroelectric Properties

The ferroelectric properties, i.e., remnant polarization (P_r), saturated polarization (P_s) and coercive field (E_C) are measured by the polarization versus electric field (i.e. by Sawyer Tower circuit), also called P-E loop. Fig.4.8 shows P-E loop of all $BaTiO_3$ samples sintered at 1100^0C, 1200^0C and 1300^0C. The ferroelectric nature of the sintered $BaTiO_3$ ceramics is confirmed by the development of saturated P-E loops. The prepared samples also show better crystallinity and homogeneity, which is described by the sharpness of the P-E loop [7]. The values of coercive field 'E_C' and remnant polarization 'P_r' are in good agreement with the earlier reported for all $BaTiO_3$ samples [10].

From figure, it is observed that there is a gap in the P-E hysteresis loop that can be due to the ohmic contacts of the electrodes and also due to the leakage current. The values of remnant polarization (P_r), saturated polarization (P_s) and the coercive field (E_C) are given in table 5. It is observed that the remnant polarization is high for BTO sample sintered at 1300^0C, because interfacial polarization (grain boundary) increases as the sintering temperature increases. This

means that the number of dipole moments of every domains increases as the grain size increases with increase the sintering temperature.

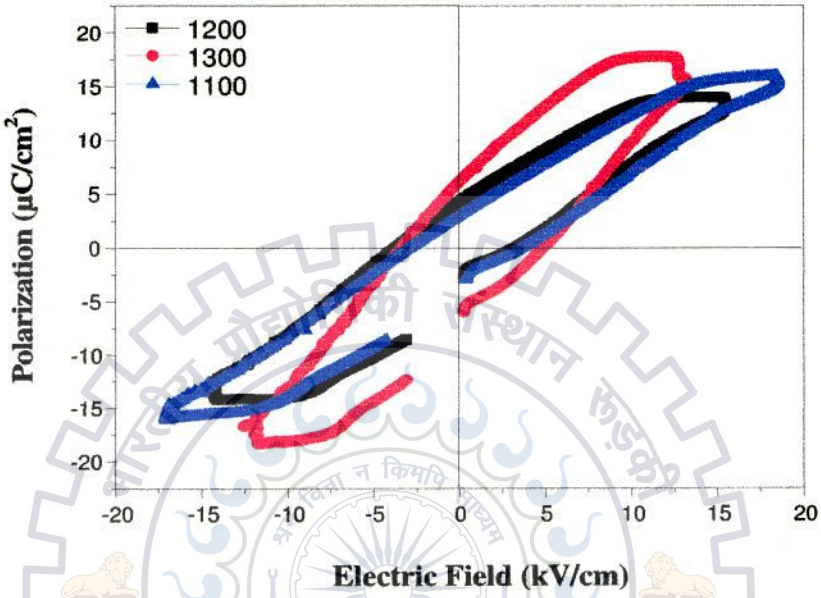

Fig.4.8 P-E loop of all $BaTiO_3$ samples prepared at different sintering temperatures.

Table 5. The values of P_s, P_r and E_C of BTO samples sintered at various temperatures

Samples	P_s (μC/ cm^2)	P_r (μC/ cm^2)	E_C (kV/ cm)
BTO 1100	16.63	3.24	2.54
BTO 1200	14.18	4.67	2.79
BTO 1300	18.25	6.64	4.28

Fig.4.9 shows the leakage current vs. time graph, that shows the stability of the materials. From figure (4.9), it is noticed that the leakage current against the time is almost constant for BTO sample sintered at 1300^0C than the other samples. This means that the BTO sample sintered at 1300^0C is more stable in comparison of others.

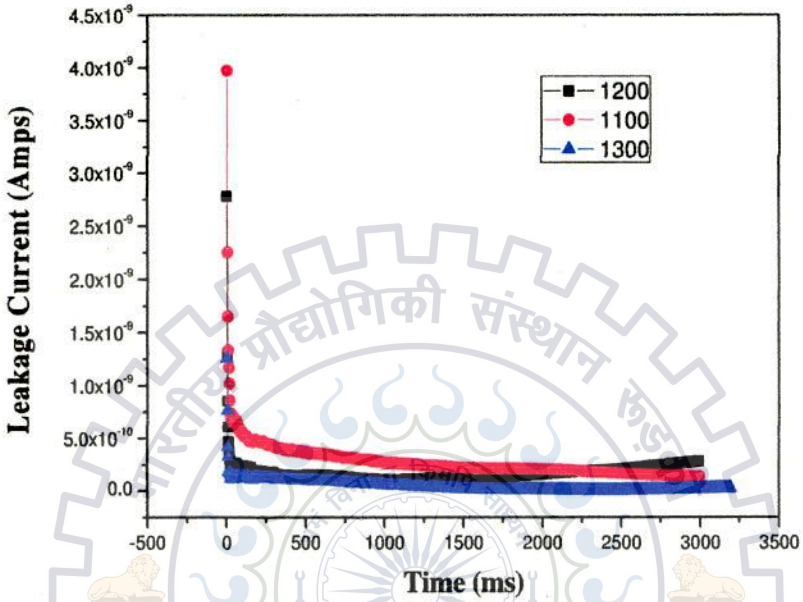

Fig. 4.9 Leakage current (Amps.) vs. time (ms) sintered at the various temperatures

It is also observed that the leakage current reduces as the sintering temperature increases and it is low for BTO sample sintered at 1300^0C. The values of the leakage current density at time zero are given in the table 6.

Table 6. Leakage current density for different samples

Samples	Leakage current density (Amp/cm^2)
BTO 1100	3.18×10^{-8}
BTO 1200	2.18×10^{-8}
BTO 1300	0.99×10^{-8}

4.2 Characterizations of the (1-x) $BiFeO_3$ - x$BaTiO_3$ composites

4.2.1 Structural Studies by XRD

The structural studies of (1-x) $BiFeO_3$ – x$BaTiO_3$ composites (i.e. x = 0, 0.1, 0.3, 0.5, 0.7 and 1.0) were carried out by an X-ray diffractometer with the Cu K_α target of wavelength (λ = 1.5406 Å). Following figures show the XRD patterns for the different composites, sintered at various temperatures. The calcinations of the prepared powder were carried out at 750^{0}C for 1 hr. The pellets are optimized at the sintering temperatures that are 870^{0}C, 980^{0}C, 980^{0}C, 1000^{0}C, 1020^{0}C and 1200^{0}C for x = 0, 0.1, 0.3, 0.5, 0.7 and 1.0 respectively. These optimized temperatures for the synthesis of these composites are determined by analyzing these XRD patterns. Formation of (1-x) $BiFeO_3$ - x$BaTiO_3$ composites were confirmed with the JCPDS database. The crystalline (1-x) $BiFeO_3$ - x$BaTiO_3$ composites are formed at these sintering temperatures.

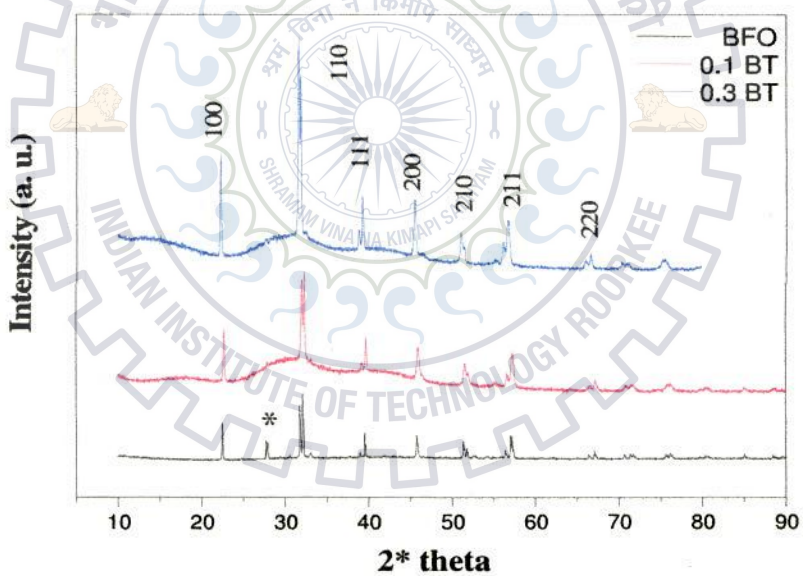

Fig. 4.10 XRD patterns of (1-x) $BiFeO_3$ - x$BaTiO_3$ ceramics with compositions, x = 0 (BFO), 0.1 and 0.3

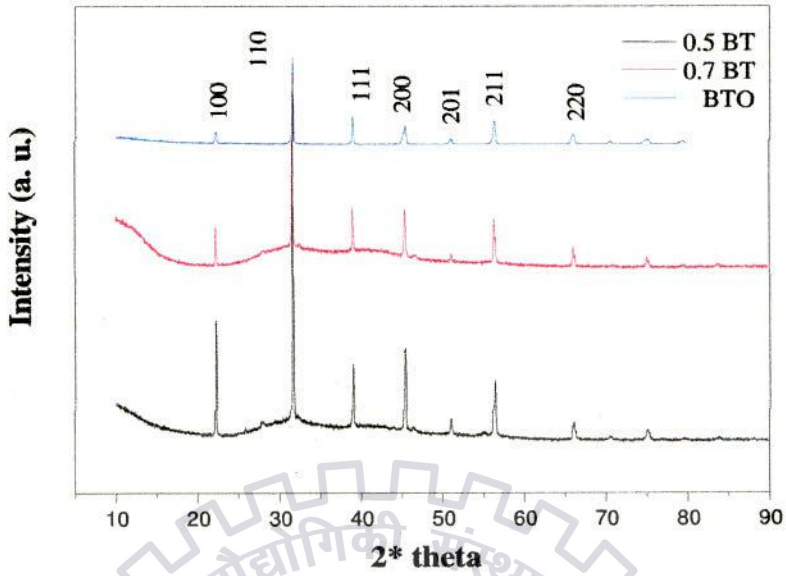

Fig. 4.11 XRD patterns of (1-x) $BiFeO_3$ - $xBaTiO_3$ ceramics with compositions, x = 0.5, 0.7 and 1.0

Figure 4.10, it is observed that a minor second phase of the possible Bi_2O_3 as indicated by '*', i.e. due to the bismuth excess (Bi_2O_3). It is proved that to prepare a pure BFO is a difficult task because of its low structural stability and relatively the low tolerance factor. As the BT concentration added the second phase is disappears, it is clear from the figure 4.11.

The XRD graph of BFO shows an observable splitting in the higher 2θ peaks that specifies a rhombohedral symmetry [11]. This splitting of the X-ray diffraction peak gradually reduces as increasing in the BT concentration and becomes almost single in 0.5BF–0.5 BT composite that indicates appearance of the cubic phase [12], shown in figure 4.12. It is also observed that XRD peaks shift towards lower 2θ positions as BT concentration increases, mainly caused by the Ba^{2+} ion has larger ionic radius (1.35 Å) in comparison of Bi^{3+} ion (1.03 Å) on the A site of the perovskite structure. While the Ti^{4+} ion (0.605 Å) and Fe^{3+} ion (0.64 Å) have the similar radii [11].

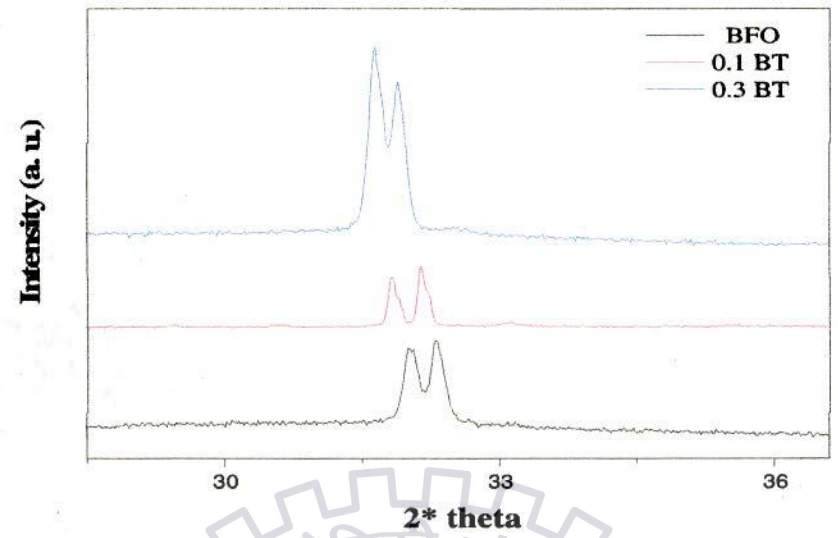

(a)

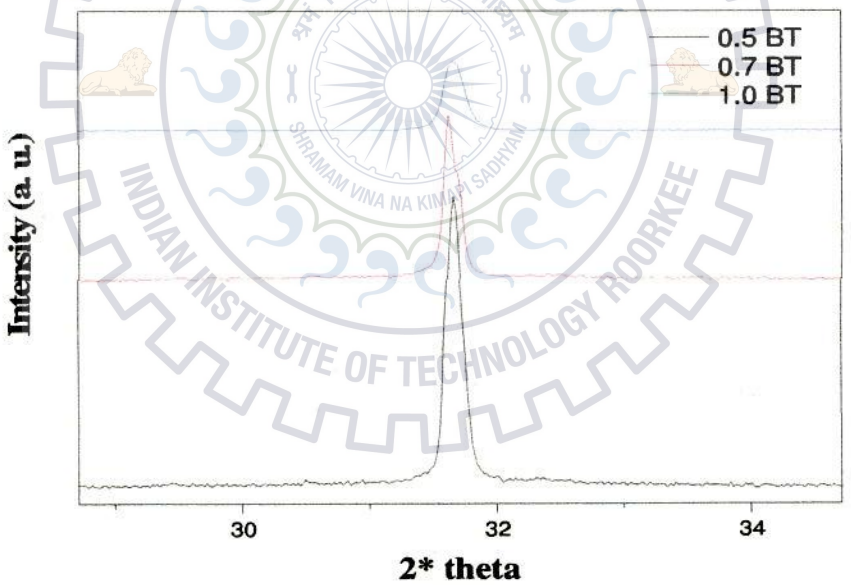

(b)

Fig. 4.12 XRD patterns at near 31.5^0 (a) for pure BFO, 0.1 BT and 0.3 BT, and (b) 0.5 BT, 0.7 BT and pure BT

From figure 4.12(a), it is observed that the intensity of the peak (h1k111) on the right side reduces and linewidth of peak (h2k212) on the left side is broadened. These changes in (h1k111) and (h2k212) peaks intensity and the broadening are due to increase of Cm phase by decreasing the BFO content [13]. For x= 1.0, i.e. pure BTO shows the tetragonal perovskite structure which is already discussed in section 4.1. The lattice constants, the angle 'α' and particle size are given in table 7.

Table 7. The values of lattice constants, angle 'α' and particle size

Samples	Lattice constants (Å)	α (degree)	Particle size (nm)
BFO	a = 3.9602	89.53	62
0.9 BF - 0.1 BT	a = 3.9672	89.71	57
0.7BF - 0.3BT	a = 3.9706	89.92	53
0.5BF - 0.5BT	a = 3.9748	90	50
0.3BF - 0.7BT	a = 3.9801	90	48
BTO	a = 3.9840, c = 4.016	90	65

It is clear that the lattice constants and distortion angle 'α' are increasing with increasing in the BT content due to the lattice expansion and the structure distorted from rhombohedral to cubic above x=0.3 BT, and cubic to tetragonal above x=0.9 [14]. It is also observed that the particle size decreases as the BT concentration increases due to the radii of Ba^{2+} (1.35 Å) is different from the Bi^{3+} (1.03 Å).

4.2.2 Surface Morphology Analysis

The Surface morphology of the (1-x) $BiFeO_3$ - $xBaTiO_3$ composites was investigated by a Field Effect Scanning Electron Microscopy (FESEM) and the compositions these composites were determined by EDAX (Energy Dispersive Analysis of the X-rays). Figure 3.13 shows the

SEM micrographs of BFO, 0.9BF-0.1BT, 0.7BF-0.3BT, 0.5BF-0.5BT, 0.3BF-0.7BT, and BT respectively.

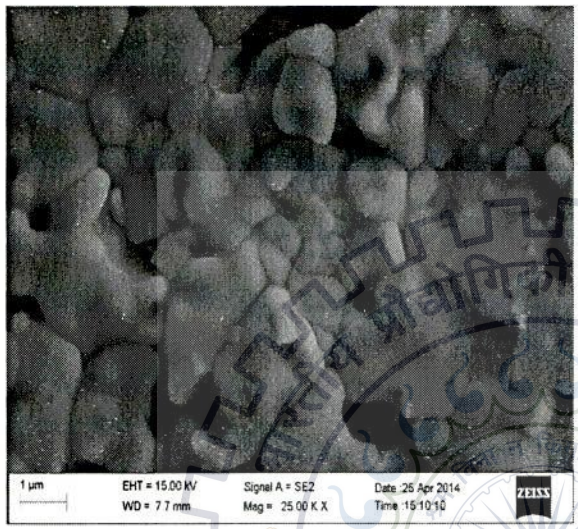

(a)

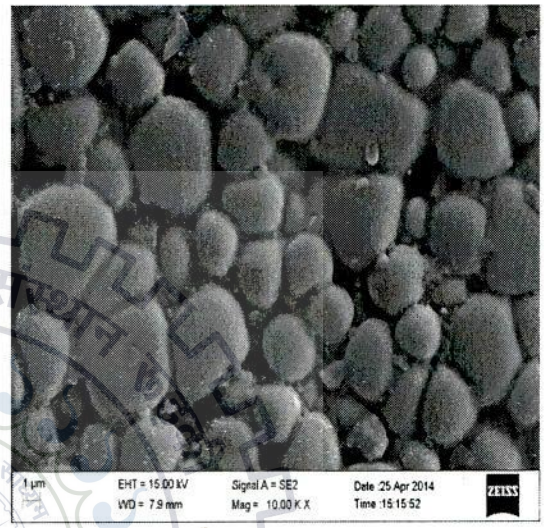

(b)

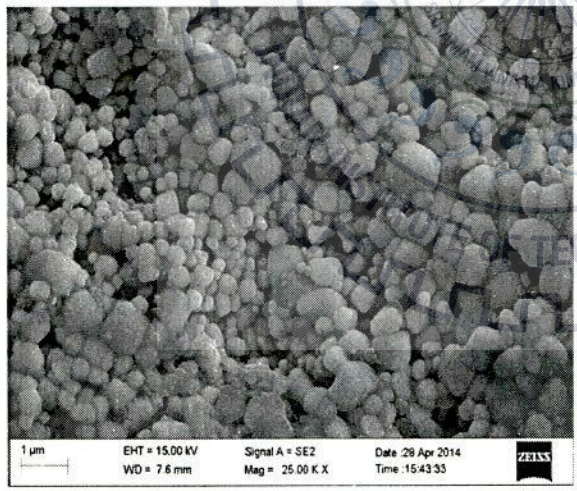

(b)

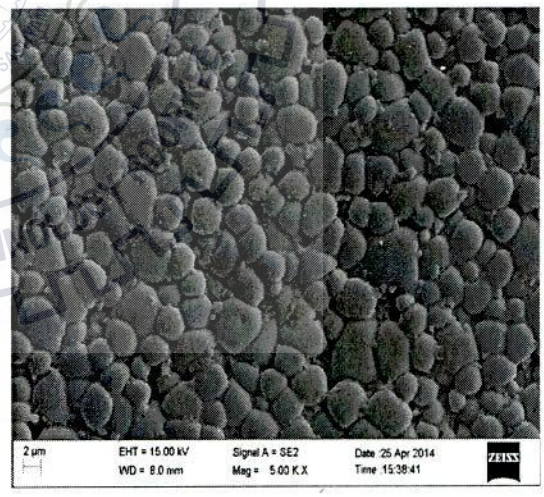

(d)

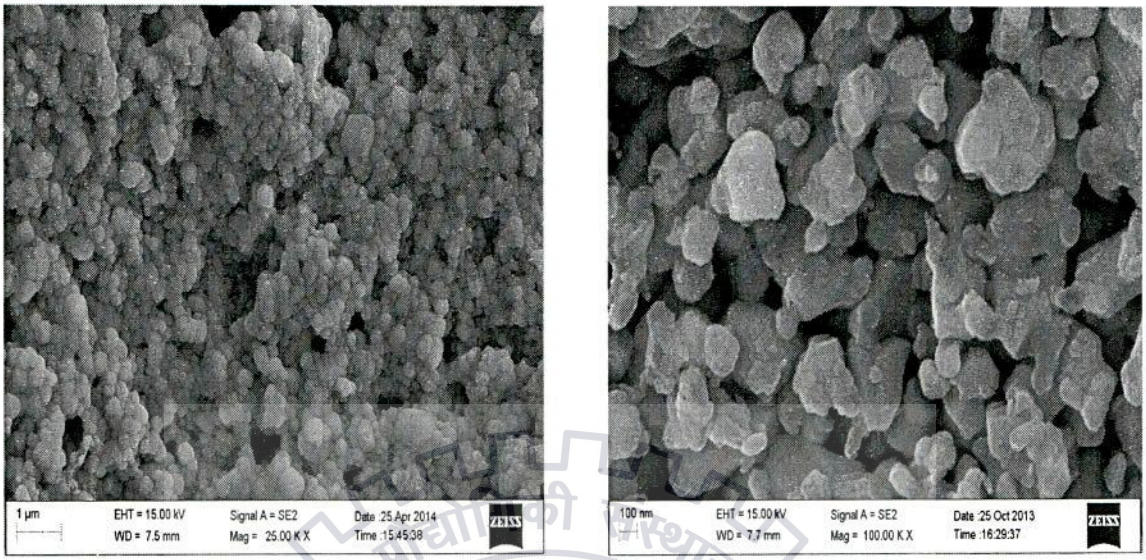

(e) (f)

Fig.4.13 SEM micrographs of (1-x) $BiFeO3$ - $xBaTiO_3$ composites at (a) x = 0, (b) x = 0.1, (c) x = 0.3, (d) x = 0.5, (e) x = 0.7, and (e) x = 1.0

The FESEM micrographs revealed that the average grain size increases with increasing of sintering temperature from 870^0C to 980^0C as shown in figure 4.13 (a) and (b). In case of 0.7 BF - 0.3 BT composite, the average grain size decreases due to substitution of larger radii Ba^{2+} (1.34 Å) atoms instead of Bi^{3+} (1.03 Å) atoms, but in case of 0.5BF – 0.5BT composite the average grain size increases as compared to the 0.7 BF - 0.3 BT composite, this could be due to the Ba^{2+} and Bi^{3+} are of same compositions and the atoms of Ba^{2+} and Bi^{3+} sit completely into each other. Further, increasing the BT content in the composite the average grain size decreases. This reduction in grain size with increasing BT content (i.e. from x = 0.5 to 1.0) is credited to the lower grain growth rates and slowly diffusion of the Ba^{2+} ion. Moreover, the 0.5BF- 0.5 BT composite shows the better homogeneity and high densification compared to the other compositions.

The values of average grain size of all compositions are given in table 8.

Table 8. Average grain size for all compositions

Samples	Average grain size (μm)
BFO	1.904
0.9BF – 0.1BT	2.712
0.7BF-0.3BT	0.855
0.5BF-0.5BT	3.059
0.3BF-0.7BT	0.564
BTO	0.450

4.2.3 Dielectric Properties

The dielectric properties (i.e. dielectric constant 'ε_r' and dielectric loss 'tanδ') are measured by the impedance analyzer with the temperature for all compositions. Fig.3.14 shows ε_r with the temperature for all compositions. From figure 4.14, it is clear that the dielectric constant has almost constant values with the temperature for all composites since the transition temperature is high for all samples except the BT.

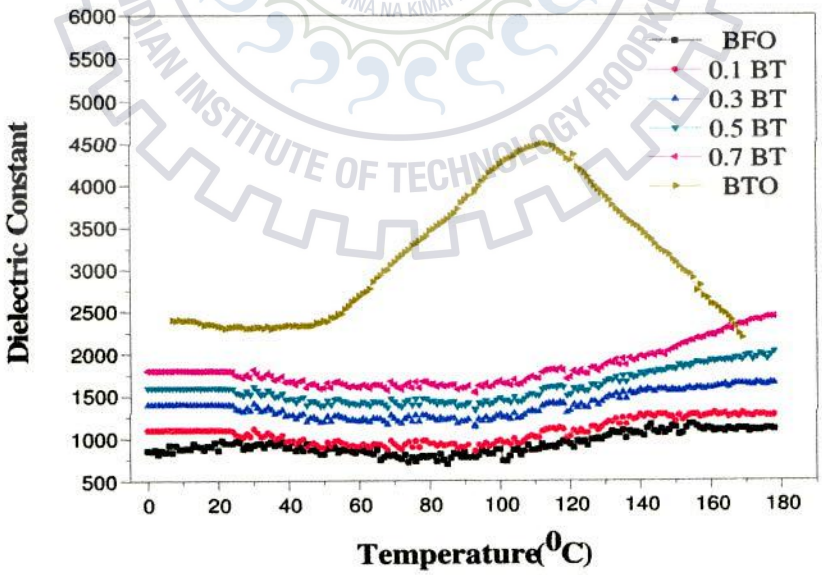

Fig. 4.14 The dependence of dielectric constants with temperature for all compositions

From dielectric behavior it is also noted that the 'ε_r' with temperature is constant and after 160^0 it increases for 0.3 BF–0.7 BT, this means that the transition temperature (i.e. ferroelectric temperature) for pure is 1103K, and when BT content is added to the BF it decreases. The dielectric constant increases from ~ 800 in BFO to ~ 1800 in 0.3BF–0.7BT and maximum ~ 2500 for BTO ceramic for frequency 1 MHz.

The dielectric loss (tanδ) vs. temperature behavior for all compositions is given in figure 4.15. The tanδ decreases as the BT content increases with the temperature.

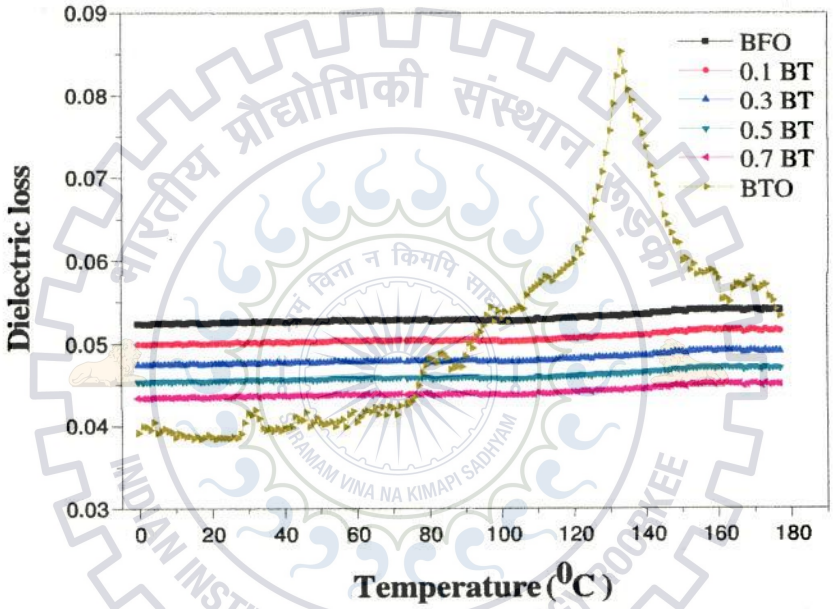

Figure 4.15 Dependence of dielectric loss (tanδ) with the temperature for all compositions.

The dielectric loss for BFO is ~ 0.053, it decreases and becomes ~ 0.043 for 0.3BF – 0.7BT. And for pure BTO, its value is about 0.038. The values of dielectric constant (ε_r) and dielectric loss (tanδ) are given in table 9.

Table 9. Dielectric constant and dielectric loss at room temperature

Samples	ε_r at RT	tanδ at RT
BFO	800a	0.053
0.9BF-0.1BT	1050	0.05
0.7BF-0.1BT	1300	0.047
0.5BF0.5BT	1600	0.045
0.3BF-0.7BT	1800	0.043
BTO	2500	0.038

The transition temperatures for all compositions are given in figure 4.16, which are determined by Differential Thermal Analysis (DTA). It is observed that the one endothermic peak appears with increasing the temperature corresponding to ferroelectric transition. As the increasing BT content ferroelectric transition peak becomes sharp and sharper for 0.3BF – 0.7 BT composite that indicates the stronger ferroelectric response cause by BT substitution. These temperatures at the peaks are determined as the Curie temperature (T_C). It is observed that the transition temperature for BFO is ~ 846^{0}C; it decreases with increasing the BT content and becomes ~ 835 for 0.3BF – 0.7 BT composite.

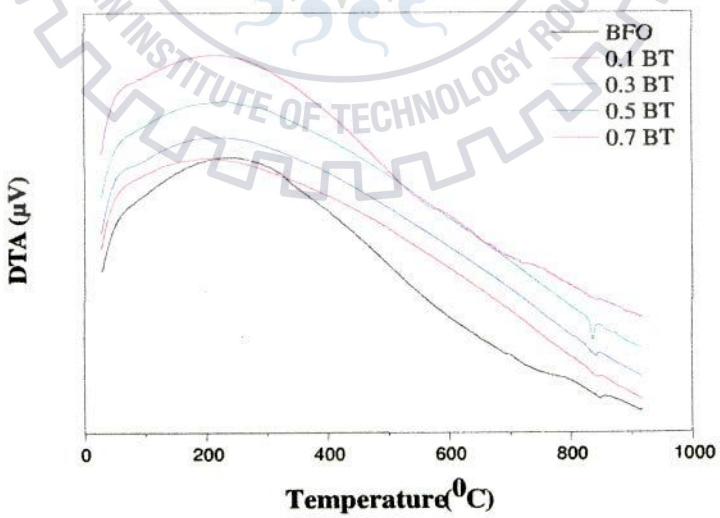

Fig.4.16 Differential thermal analysis graph

From DTA graph, it is clear that there is a small change in the transition temperature with increasing BT content.

4.2.4 Ferroelectric Properties

The ferroelectric measurements are carried out by the hysteresis P-E loop. The ferroelectric loops of polarization (P) vs. electric field (E) for the BFO−BTO ceramics at room temperature are shown in figure 4.17 (a)− (f). All the compositions show the ferroelectric hysteresis loops.

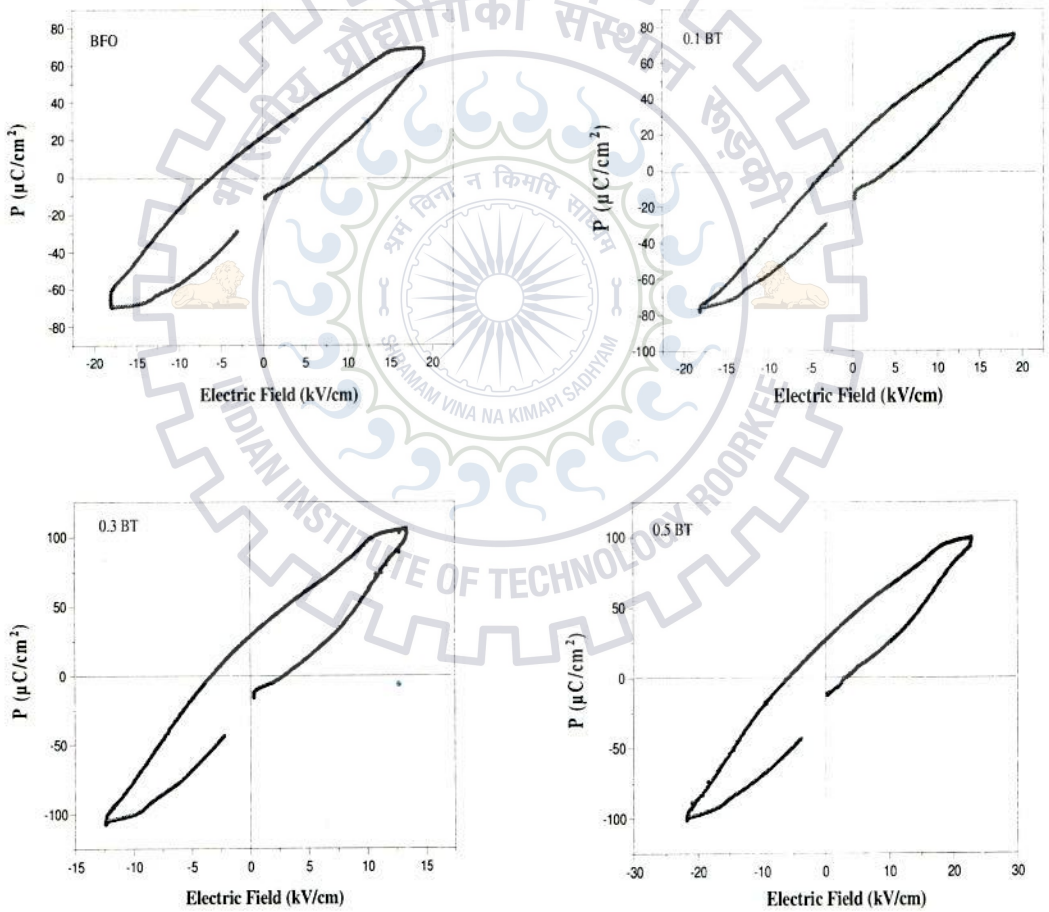

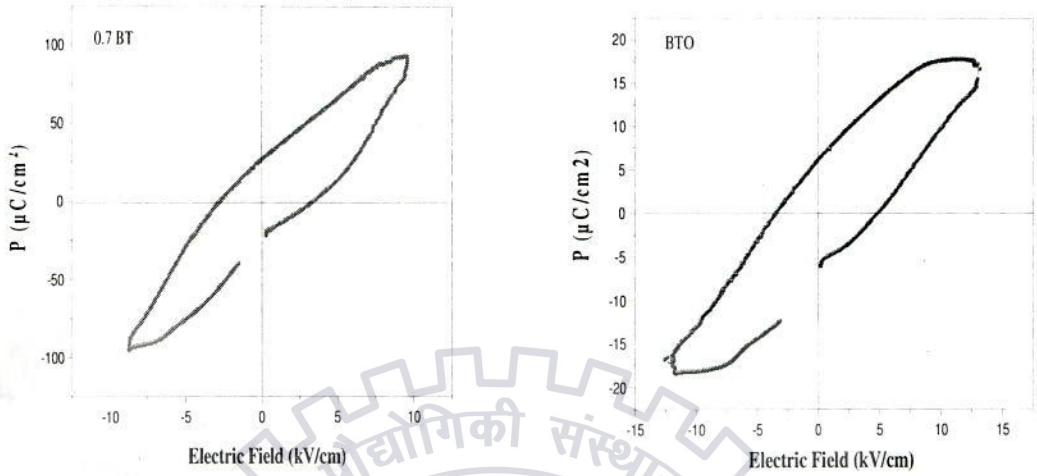

Fig.4.17 Hysteresis loops of polarization (P) vs. electric field (E) for (a) x=0, (b) x=0.1, (c) x=0.3, (d) x=0.5, (e) x=0.7, and (f) x=1.0

From figure 4.17, it is observed that the ferroelectric hysteresis loops become slimmer with the substitution of BT content from x=0.1 to 0.5, after that it becomes broader. This means that the polarization induced by the electric field reduced quickly when electric field decreases to zero. The slimmer ferroelectric loops are observed in the relaxor ferroelectric materials.

It is also clear that the remnant polarization first increases, which is highest for 0.3 BT and after that it starts to decrease with the increasing BT content. Among all the compositions, 0.7BF–0.3BT ceramic shows highest remnant polarization $P_r \sim 28.9\ \mu C/cm^2$. Similar results are also found in the literature, where the polarizations are low [13]. It is clear that from the hysteresis loops, this behavior is intimately related with structural evolution of BF – BT composites. As discussed already, in this system, coexistence of the two mechanisms for the ferroelectricity that leads to coexistence of the two distinct structural symmetries. For high BF contents, the structure is rhombohedral and the polarization is low, as the BT concentration increases the Cm symmetry became dominant which allows the high polarizations. Further, the addition of BT content causes a symmetry increase and a reduction in polarization figure 3.19

(e). The remnant polarization (P_r), saturated polarization (P_s) and the coercive field (E_C) are given in the following table.

Table 10. The values of P_r, P_s and E_C

Samples	P_r ($\mu C/cm^2$)	P_s ($\mu C/cm^2$)	E_C (kV/cm)
BFO	20.80	69.97	3.91
0.9BF-0.1BT	14.93	75.47	3.78
0.7BF-0.3BT	28.90	104.98	2.88
0.5BF-0.5BT	27.81	99.85	3.55
0.3BF-0.7BT	26.23	91.99	3.89
BTO	6.64	18.25	4.28

It is also observed that the saturated polarization (P_s) and the coercive field (E_C) increases as the BT content increases, maximum for 0.7BF−0.3BT, and starts to decrease with increasing the BT content. Fig.4.18 shows the leakage current (in amps) behavior with time (in ms) that indicates the stability of the samples.

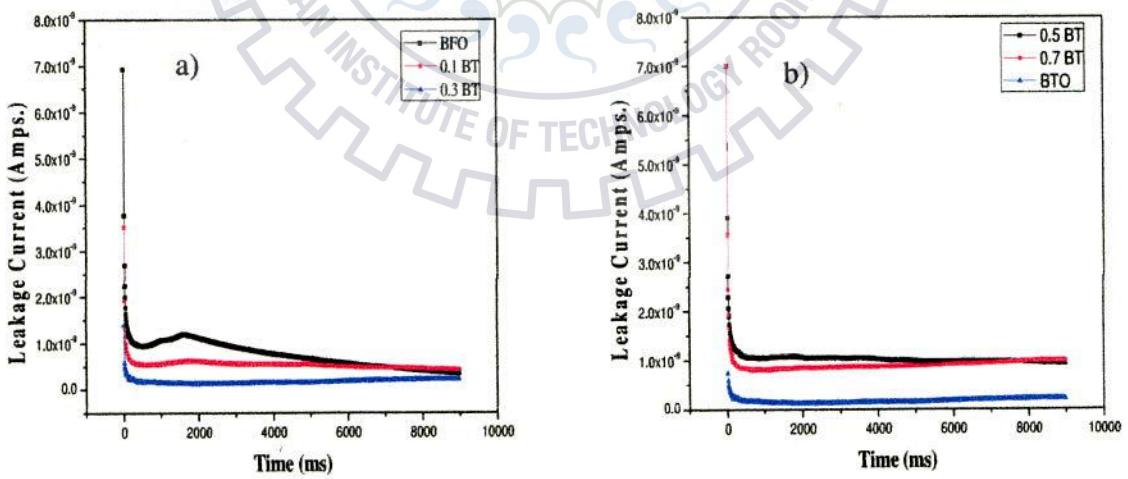

Fig. 4.18 Leakage current versus time of (1-x) BF−x BT ceramics (a) at x=0, 0.1, 0.3 and (b) at x=0.5, 0.7, 1.0

From figure 4.18, it is clear that the structural stability for the BFO sample is low, because the behavior of leakage current with the time is not constant, but other than this the leakage current behavior with the time is constant. It is also found that the leakage current density starts decrease as the BT content increases, and it is high for 0.3 BT–0.7 BT and also for pure BTO. This means that the stability of the samples increases as the BT concentration increases.

REFERENCES:

[1]. Wei Cai, etal. Integrated Ferroelectrics, 105: 1–10, 2009.

[2]. K.R. Kambale et al. / Ceramics International, 2013.

[3]. F. J. Humphreys and M. Hatherly (1995); *Recrystallization and related annealing phenomena.*

[4]. Dinghua Bao. Journal of Physics D Applied Physics, 2002.

[5]. Sonia et al. / Ceramics International 38 (2012) 1585–1589.

[6]. Maruthi, G.; Kumari, R. Ananda and Chandramani, R. "Investigations on Non Linear Optical Crystal ADP Doped with Inorganic Compounds", International Journal of ChemTech Research, 2011.

[7]. O.P. Thakur, C. Prakash, D. Agrawal, Structural and electrical properties of microwave processed BaTiO3 ceramic, Int. J. Ceram. Process. Res. 3 (2) (2002) 75.

[8]. B. Jaffe, W.R. Cook, Piezoelectric Ceramics, Academic Press, London, U.K., 1971.

[9]. G.H. Heartling, Ferroelectric ceramics: history and technology, J. Am. Ceram. Soc. 82 (1999) 797.

[10]. Sonia et al. / Ceramics International 38 (2012) 1585–1589.

[11]. Wang, T.H. et al., Phase transition and ferroelectric properties of $xBiFeO_3$-(1-x) $BaTiO_3$ ceramics, Current Applied Physics, 2011.

[12]. M. M. Kumar, A. Srinivas, and S. V. Suryanarayana, J. Appl. Phys. 87, 855 (2000).

[13]. Gotardo et al. J. Appl. Phys. 112, 104112 (2012).

[14]. Yang et al. J. Appl. Phys. 113, 144101 (2013).

The structural, dielectric and ferroelectric properties of $BaTiO_3$ (BTO) were investigated, which is prepared by the solid state reaction method. It is found that the BTO ceramics sintered at 1100^0C, 1200^0C and 1300^0C possess pure perovskite single phase tetragonal structure, which is confirmed by the XRD analysis. The average grain size increased from 0.3 μm to 0.6 μm as the sintering temperature increases. The BTO ceramic sintered at 1300^0C shows the dense, homogeneous, pore free and the uniform microstructure, which suggests the advantage of using high temperature sintering. The dielectric constant is high (~ 4200) and dielectric loss is low (~ 0.05) for BTO sample sintered at 1300^0C. The ferroelectric properties are also enhanced for BTO samples sintered at 1300^0C and its value ~ 6μC/cm^2.

(1-x) BFO – x BTO (x=0 – 1.0) ceramics were prepared by solid state reaction method. The impurity peaks of a second phase disappeared with the increasing of the BTO content. The coexistence of rhombohedral and cubic perovskite structure was observed in BFO–BTO ceramics as the BTO concentration increases, it is due to contention in the two different mechanisms liable for the ferroelectricity in the BFO–BTO composites. As BTO increases the cubic phase gets major and approaches to tetragonal structure for high above ~ 90% of BTO concentration. The dielectric constant rises and Curie temperature 'T_C' decreases as BTO concentration increases. Average grain size shows an increasing trend as the BTO concentration increased from x= 0–0.1 and then reached a maximum value at x=0.5 and for a concentration ranging from x=0.5-1.0, the average grain size shows a gradual decrease. For x=0.5, the microstructure is uniform, homogeneous, pore free and dense. The polarization is also affected by the substitution of BTO and it has maximum value (~ 29μC/cm^2) for 0.7 BFO–0.3 BTO composite.